



Morphological stability of steady-state passive oxide films

Rohit Ramanathan, Peter W. Voorhees*

Department of Materials Science and Engineering, Northwestern University, Evanston, IL 60208, USA



ARTICLE INFO

Article history:

Received 2 October 2018
 Received in revised form
 23 January 2019
 Accepted 25 January 2019
 Available online 4 February 2019

Keywords:

Corrosion
 Passivity breakdown
 Morphological stability
 Point defect model
 Linear stability

ABSTRACT

Understanding the kinetics of passive oxide formation and breakdown has been an ongoing problem for corrosion scientists for several decades. Here, we present a model for the formation of a passive oxide film on a metal that is an extension of the Point Defect Model (PDM) by Macdonald and coworkers. We replace the potential description of the PDM with a boundary value problem and ensure that Gauss's law is satisfied at the oxide-solution interface by considering the presence of the Helmholtz layer in solution. Our model predicts the observed linear variation of the steady-state film thickness with anode potential, and an increasing film thickness with increasing pH. We perform a linear stability analysis of the model and show that, depending on the parameters, the passive film may be unstable to morphological perturbations of the film interfaces, leading to nonplanar films and potentially the formation of a pit in the oxide. This also implies that one-dimensional models, which assume planar interfaces, can be inapplicable in broad classes of corrosion processes. The analysis shows that a morphological instability exists if the oxide dissolution mechanism is such that an increasing Helmholtz layer potential drop leads to an increasing dissolution rate. The instability behavior is consistent with the literature on breakdown of passivity in the presence of chloride ions. The theory provides insights on the initiation of passivity breakdown leading to pitting corrosion and the role that interfacial energy plays in determining stability.

© 2019 Elsevier Ltd. All rights reserved.

1. Introduction

Metals can protect themselves from corrosion by forming passive oxide films on their surfaces. However, the corrosion resistance conferred by the presence of a passive oxide film may not exist indefinitely. Under certain conditions it is possible for this film to break down locally, leading to pitting corrosion of the underlying metal. Pitting corrosion is extremely difficult to model and predict, and can lead to premature failure of a part while it is in service. Several factors influencing the breakdown of the passive film have been identified, including chloride concentration and local pH [1]. However, there is no generally accepted mechanism for the breakdown of the film, and several competing models exist that include disparate effects such as chloride adsorption to or incorporation into the film [2–4], Zener breakdown [5], and electro-mechanical couplings such as electrostriction and flexoelectricity [6–8].

There are many models that have been used to describe the growth and breakdown of oxide films [9–15]. An important model

that is used to explain the growth of passive films is the Point Defect Model (PDM) [3,9,10]. The strengths of the PDM are that it treats the diffusion of cations and anions through the film, along with the reactions at the interfaces. The PDM also includes dissolution of the oxide film, and thus was the first model that could account for steady-state film thicknesses. However, this model is inherently one-dimensional, and thus assumes that the metal-oxide and oxide-solution interfaces are always planar. This can be problematic if the planar interfaces are unstable to small morphological perturbations. To determine if this is the case, it is necessary to develop a two- or three-dimensional model that can follow the evolution of nonplanar interfaces. This is particularly important, since, if either of the planar interfaces are morphologically unstable, then the one-dimensional model cannot be used to describe oxide growth. Furthermore, these non-planar morphologies can grow in amplitude. When the amplitude of the perturbations approaches the thickness of the passive film, localized breakdown occurs. Thus, a two- or three-dimensional model will describe both growth of a planar film and localization, and it is not necessary to invoke a model for film growth that is based on different physics to describe localization as has been done previously [3,16,17]. Such a higher dimensional model can also be modified to include the effects of Cl^- , and microstructural

* Corresponding author.

E-mail address: p-voorhees@northwestern.edu (P.W. Voorhees).

inhomogeneities such as grain boundaries and precipitates.

From morphological stability theory, it is well-known that planar interfaces may be unstable to shape perturbations, leading to complex interface morphologies [18,19], and breakdown events [7,20]. The rapid and autocatalytic nature of film breakdown and pit formation suggests that pitting may result from an instability in the passive film itself. It is thus clear that a self-consistent morphological stability analysis of a passive film with a steady-state thickness in aqueous environments is needed. A major challenge is that existing models for passive film growth assume the form of the electrostatic potential distribution from the metal to the solution [10,11], and thus cannot self-consistently describe the evolution of non-planar interfaces. Other models [12–15], while not assuming the potential, do not include the interfacial energies of the metal-oxide or oxide-solution interfaces that are critical in determining the evolution of nonplanar films. Without interfacial energy, or its manifestation, the Gibbs-Thomson effect,¹ the evolution equations for interfacial morphologies contain unphysical singularities. Furthermore, this latter class of models are formulated for specific metal-oxide systems. While offering great insight into the passive film formation kinetics for those specific systems, it can be difficult to use them to make general conclusions about passivity.

Since morphological stability analyses of corrosion processes are uncommon, we describe the basic ideas here. A more complete description of the phenomena can be found in review papers of Langer [18] and Sekerka et al. [19]. Morphological stability refers to the stability of a particular idealized interfacial morphology, which, in our case, is a planar thin film. To understand the instability phenomenon, it is helpful to consider the case of unidirectional solidification into an undercooled liquid. In unidirectional solidification, as with passive film growth, there is a one-dimensional model that describes the composition fields in the solid and liquid, with the implicit assumption that the solid-liquid interface is planar. However, the planar interface can be unstable to small shape perturbations, leading to the solid-liquid interface becoming nonplanar, and implying that the one-dimension solidification model is not physically relevant. The small shape perturbations, when unstable, can develop into cells or dendrites. The shape perturbations grow as a result of the diffusion field in the liquid, but are opposed by interfacial energy that tends to planarize the interface through capillarity [19].

A wide variety of morphological instabilities have been identified, all of which are a result of the competition between some destabilizing driver (diffusion field [19], electric field [20], stress [21,22], or magnetic field [23]) and the stabilizing driver, interfacial energy. Morphological stability theory provides a rigorous framework through which the development of these complex interface shapes can be described. In a morphological stability analysis, the dynamics of the non-planar interface are cast in terms of a small-amplitude, fixed-wavelength perturbation of the idealized interface shape. Evolution equations for the shape perturbations are derived from the global evolution equations, which allows for the growth rate of the perturbations as a function of their wavelength to be identified. The morphological instability approach is powerful in that it allows for the determination of mechanisms that lead to instabilities, allowing one to identify what factors are important or unimportant in determining morphology, as well as the size and time scales of the instability. As noted by Okada [24], the morphological stability analysis corresponds to an *a posteriori*

approach, where we acknowledge the existence some perturbation of the passive film interfaces (the source of the perturbation is left unspecified), and examine how that perturbation evolves. The perturbation could be due to, for example, thermal noise or small microstructural inhomogeneities in the metal or oxide.

A few morphological stability analyses of passive oxide films have been performed. Wagner considered the stability of a non-planar oxide growth front and found that if diffusion in the alloy is slower than in the oxide, the oxide will be nonplanar and rough [25]. Okada analyzed the stability of passive film dissolution by considering perturbations of the transport processes in solution [24]. He explicitly included chloride adsorption to the oxide surface, and found an instability whose growth rate increased with increasing chloride concentration. However, these two analyses neglected to consider how interfacial energy stabilizes the planar interface shape [26]. Without the addition of this effect, the growth rate of the instability diverges nonphysically to infinity as the wavelength of the perturbation decreases. Furthermore, these analyses only consider perturbations of one of the oxide interfaces, despite the fact that in aqueous environments, both interfaces are moving [10,13]. Thus, it was not possible to consider whether the instability at one interface affects the stability of the other interface.

Singh et al. [27,28] and Stanton et al. [29,30] recognized the importance of interfacial energy in their analyses of the linear stability of anodic alumina growth. In this case, they consider the influence of an “activation surface energy” on the reaction rates at both film interfaces. It must be noted that this is *not* the macroscopic surface (interface) energy, but is a quantity associated with the energy of the transition state for the interface reactions [31]. Furthermore, some authors [6,8], while not performing stability analyses, have considered the stabilizing influence of a “surface energy stress” by including a term γ/L where γ is the interface energy and L is the planar film thickness. While having the same units as stress, there is no stress associated with surface energy for a planar surface. Surface energy only becomes relevant to describing morphological evolution when the surfaces are curved. A surface stress (which differs from surface energy) will lead to a bulk stress in the film if the surface has non-zero curvature [32].

The focus of this work is to develop and analyze the morphological stability of a model for passive film growth. The model we formulate is an extension of the Point Defect Model (PDM) [9,10] where we replace the assumed electrostatic potential distribution with a boundary value problem and ensure that Gauss's law is satisfied at the oxide-solution interface. We analyze the linear stability of the model to simultaneous shape perturbations of the metal-oxide and oxide-solution interfaces and identify the conditions under which the film is unstable and breakdown may occur. Our analysis explicitly considers the influence of interfacial energy through the Gibbs-Thomson effect, as well as two models for the dissolution of film at the oxide-solution interface. The instability mechanism we find is consistent with the localized thinning mechanism for pitting proposed in the literature [1,16,33]. From the theory presented, we are able to give an indication of *both* the size and time scales for the breakdown event. Previous models for passivity breakdown have focused on the mechanism, while not elucidating a size or time scale for breakdown.

2. Review of models for passive film growth

Several models for the growth of passive films exist, and we begin by reviewing two of them here to discuss to the features of the problem that need to be included in a realistic growth model. All of the models recognize that during oxide growth, an electric field exists across the film that drives the motion of charged defects leading to growth of the film either at the metal-oxide interface (if

¹ the Gibbs-Thomson effect accounts for how the chemical potential of a component is modified by the presence of a curved interface with interfacial energy.

interface should evolve during growth. We formulate the potential in the system as a boundary value problem, so that the evolution of the electric field and the oxide-solution potential drop occur simply as a consequence of the boundary conditions at the passive film interfaces. The model we formulate consists of three submodels: a model for the potential distribution from the anode to the solution, a model for the transport of cation and anion vacancies in the film, and a model for the kinetics of the passive film dissolution reaction (reaction 5 in Fig. 1).

In this section, we develop the model and its boundary conditions for the most general case of a three-dimensional passive film with nonplanar interfaces. In Section 4, we solve the model equations for the basic state corresponding to a passive film with planar interfaces. In Section 5, we perform the morphological stability analysis and identify the conditions under which non-planar morphologies are to be expected.

3.1. Coordinate system

Before describing the model equations, we must first define the coordinate system of interest. This is because when a passive film exists with the steady-state film thickness, the boundaries of the film are not stationary, but are both moving toward the metal at a constant velocity, V , relative to an observer in the lab. The coordinate system that we choose is shown in Fig. 2. We fix the metal-oxide interface at $x = 0$. The oxide-solution interface has variable position $x = L(t)$ in the general case where the film is growing. When the steady-state is achieved, $L(t)$ becomes fixed in time. In this section we will define the model equations in this frame of reference. Prior to solving the equations in Section 4 we will cast them to the moving reference frame where the film boundaries are fixed in the steady-state.

3.2. Potential

Consider a system consisting of a metal, oxide, and solution as shown in Fig. 2. A physical requirement missing from the PDM and GGM is that Gauss's law must be satisfied at the oxide-solution interface. To accomplish this, we follow the approach of Dewitt and Thornton [14], and separate the potential into two parts: the potential in the oxide, ϕ_O , and the potential in the Helmholtz layer in solution, ϕ_H . We assume that the potential drop through the Helmholtz layer is linear, which implies that the layer contains no

net charge and thus $\nabla^2 \phi_H = 0$. The Helmholtz layer has fixed thickness δ_H ; its boundaries lie at $x = L(t)$ and $x = L(t) + \delta_H$. The potential is continuous at the oxide-solution interface, or $\phi_H(L(t)) = \phi_O(L(t))$. For convenience, we set the potential of the bulk solution to be zero, or $\phi_H(L(t) + \delta_H) = 0$.

For the potential in the oxide, ϕ_O , we assume that the film is charge neutral and thus $\nabla^2 \phi_O = 0$. At the metal-oxide interface, we fix the potential as $\phi_O(0) = V_A - \Delta\phi^{M/O}$, where V_A is the applied anode potential relative to the bulk solution potential. $\Delta\phi^{M/O}$ is the potential drop at the metal-oxide interface, which we assume to be a constant as in the GGM [11]. We assume that the oxide-solution interface is not charged, and we require Gauss's law to be satisfied. Thus, the boundary condition at the oxide-solution interface is:

$$\frac{\partial \phi_H}{\partial n_2} - \epsilon^r \frac{\partial \phi_O}{\partial n_2} = 0 \text{ at } x = L(t) \quad (1)$$

Here, $\partial \phi / \partial n_2 = \nabla \phi \cdot \mathbf{n}_2$, where \mathbf{n}_2 is the oxide-solution interface normal vector, shown in Fig. 2. $\epsilon^r = \epsilon_O / \epsilon_H$ is the ratio of the dielectric constants of the oxide and Helmholtz layer. By including the Helmholtz layer in the solution, the oxide-solution potential drop, $\Delta\phi^{O/S}$ does not need to be specified separately and is a natural result of the model. Since the Helmholtz layer is considered part of the interface, $\Delta\phi^{O/S} = \phi_O(L(t)) - \phi_H(L(t) + \delta_H) = \phi_O(L(t))$.

3.3. Transport

The transport model that we employ is virtually identical to that in the original PDM [9,10], as we utilize the set of reactions given in Fig. 1. We also assume that reactions (1), (2), (3), and (4) in Fig. 1 are in equilibrium at a given potential drop. We use the Nernst-Planck equation

$$\mathbf{J}_j = -D_j \nabla C_j - \frac{D_j z_j \mathcal{F}}{RT} C_j \nabla \phi_O, \quad j = \text{V}_O, \text{V}_M^+ \quad (2)$$

to describe the fluxes of cation and oxygen vacancies in the oxide. Here, D_j , C_j , and z_j are, respectively, the diffusion coefficient, concentration, and charge number of species j . \mathcal{F} is Faraday's constant, R is the gas constant, and T is temperature. The linear Nernst-Planck equation assumes a small potential gradient (electric field) in the

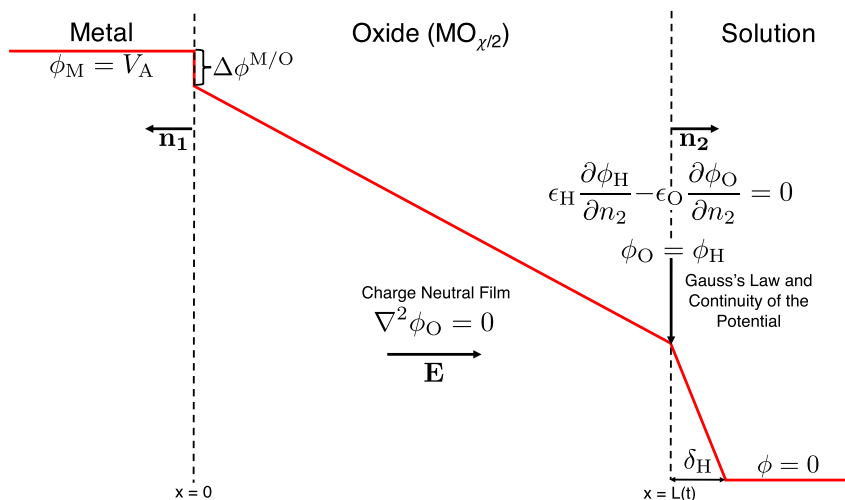


Fig. 2. Distribution of the potential from the anode to the solution. The governing equations for the potential are shown in the diagram, as well as the boundary conditions.

oxide, which may not be true for these very thin passive films. The Fromhold-Cook nonlinear flux equation [39] is likely more appropriate but makes obtaining analytical solutions very difficult. We further assume that diffusion occurs under quasi-steady conditions and thus $\nabla \cdot \mathbf{J}_j = 0$.

The primary change that we make to the transport model is that we reformulate the boundary conditions in order to satisfy structure conservation in the oxide and account for the Gibbs-Thomson effect at nonplanar interfaces. Structure conservation is the requirement that the number of cations and cation vacancies must equal the total site density on the cation sublattice, the same being true for oxygen anions and vacancies [40]. The structure conservation requirement ensures that the vacancy concentrations are bounded between 0 and 1 mol. frac. This change was needed to avoid calculating vacancy concentrations that exceed the site density of the appropriate oxide sublattice using the boundary conditions in the original PDM [9,10]. This is because in the PDM, no activity correction is made to the chemical potentials of the species M_M and O_O , only the activities of vacancies are considered. The second change that we make is to add a Gibbs-Thomson correction to the chemical potentials of cation and anion vacancies at the interfaces in order to account for how interfacial energy and curvature modify the defect concentrations.

Our boundary conditions are listed in Table 1, and are formulated by assuming an ideal solution model for the chemical potentials of species in the oxide. We further assume that the partial molar volumes of cation and oxygen vacancies are the same and equal to \bar{V} . The $\Delta\mu_i^\circ$ values are calculated assuming the reactions proceed from left to right as written in Fig. 1. In these boundary conditions the presence of $C_j/(1 - C_j)$ ensures structure conservation, while the $\bar{V}\gamma\kappa$ term accounts for the Gibbs-Thomson effect. Appendix A gives a derivation of the boundary condition for the cation vacancy concentration at the metal-oxide interface. The other boundary conditions are derived similarly. The boundary conditions in Table 1 can be shown to be equivalent to those given in the original PDM if the defect concentrations are less than $\approx 10^{-2}$ mol. frac and the curvatures, κ_1 and κ_2 are taken to be 0.

3.4. Passive film dissolution

The final piece of the model is a description of how the passive film dissolves into solution. Dissolution of the passive film is necessary in order for the film to achieve a steady-state thickness. The prevailing view is that the passive film is far from the dissolution equilibrium of the Pourbaix diagram, and the dissolution reaction can be considered to be irreversible [10,33,41]. The dissolution rate is usually written in Butler-Volmer form, which recognizes an explicit dependence of the rate on the oxide/solution

potential drop. The dissolution reaction (reaction 5 in Fig. 1) gives the net reaction that corresponds to movement of the oxide-dissolution interface. This reaction may or may not proceed as a single step, and the rate law has a strong dependence on the mechanism considered. Unfortunately, dissolution of the passive film cannot be posed in universal terms, since the dissolution mechanism will depend strongly on the oxide considered and solution chemistry as noted in Ref. [13].

We delineate two cases that plausibly describe the dissolution reaction rate. The first case comes from the PDM [10] in which the overall dissolution reaction $M_M + \frac{\chi}{2} O_O + \chi H^+ \rightarrow M^{\delta+} + \chi H_2O + (\delta - \chi)e^-$ is used to write a Butler-Volmer rate law. The PDM assumes the dissolution reaction occurs as a single step, and thus the number of electrons involved in the reaction corresponds to the net charge transferred across the interface. For a single step reaction, the reaction orders correspond to the stoichiometric coefficients, and the PDM dissolution rate, J_d^P , is

$$J_d^P = k_d^P C_{M_M} C_{O_O}^{\chi/2} C_{H^+}^{\chi} \exp\left(\frac{\alpha(\delta - \chi)\mathcal{F}\Delta\phi^{O/S}}{RT}\right) \quad (3)$$

where k_d^P is the PDM dissolution rate constant and α is the charge transfer coefficient. In this case, if $\delta = \chi$ (e.g. NiO dissolution [42]), the dissolution rate will not depend on the oxide-solution interface potential drop.

A second model of oxide dissolution is worth considering as well, since several authors have noted a potential dependence to the film dissolution rate, even if the cation charge does not change when it is ejected into the solution, in contrast to the rate law used in the PDM. For example, potential dependent dissolution has been noted by Vetter [41] and Sato [43] for the passive films on iron and nickel respectively. Vetter, when examining the dissolution of the oxide film considers it to be a multi-step process where the release of the cation into solution is the rate limiting step [41]. In his analysis, the charge of the cation in solution, δ , corresponds to the net charge transferred across the interface. Thus, the dissolution rate will always depend on the potential drop at the oxide-solution interface, unless a neutral metal atom is ejected into solution. The dissolution rate for the Vetter mechanism, J_d^V , is

$$J_d^V = k_d^V C_{M_M} C_{H^+}^{\chi} \exp\left(\frac{\alpha\delta\mathcal{F}\Delta\phi^{O/S}}{RT}\right) \quad (4)$$

where k_d^V is the Vetter dissolution rate constant. We will consider the behavior of our model for the two plausible dissolution rates, J_d^P and J_d^V . The concentrations of oxygen and metal appearing in Eqs. (3) and (4) are functions of the potential drop and the curvature of

Table 1

Concentration boundary conditions for solving the transport equations. $\Delta\mu_i^\circ$ is the standard state free energy change for reaction i , where i corresponds the interfacial reaction as numbered in Fig. 1. $a_{M^{i+}}$ is the activity of cations in solution. $\gamma^{M/O}$ and $\gamma^{O/S}$ are the energies of the metal-oxide and oxide-solution interfaces, respectively. κ_1 and κ_2 are the curvatures of the metal-oxide and oxide-solution interfaces. These boundary conditions correspond to the concentrations in mole fraction.

Interface	Species	Boundary Condition
Metal-Oxide	Oxygen Vacancy	$(1 - C_{V_M})C_{V_O} = \exp\left(\frac{-\Delta\mu_1^\circ + 2\mathcal{F}\Delta\phi^{M/O} - \bar{V}\gamma^{M/O}\kappa_1}{RT}\right)$
	Cation Vacancy	$\frac{C_{V_M}}{1 - C_{V_M}} = \exp\left(\frac{\Delta\mu_3^\circ - \chi\mathcal{F}\Delta\phi^{M/O} - \bar{V}\gamma^{M/O}\kappa_1}{RT}\right)$
Oxide-Solution	Oxygen Vacancy	$10^{2pH}\left(\frac{C_{V_O}}{1 - C_{V_O}}\right) = \exp\left(\frac{\Delta\mu_2^\circ - 2\mathcal{F}\Delta\phi^{O/S} - \bar{V}\gamma^{O/S}\kappa_2}{RT}\right)$
	Cation Vacancy	$a_{M^{i+}}\left(\frac{C_{V_M}}{1 - C_{V_M}}\right) = \exp\left(\frac{-\Delta\mu_4^\circ + \delta\mathcal{F}\Delta\phi^{O/S} - \bar{V}\gamma^{O/S}\kappa_2}{RT}\right)$

the oxide-solution interface. Thus the curvature of the interface can affect the dissolution rate of the oxide.

4. Solution for a planar passive film

4.1. Film growth rate and moving reference frame

The growth rate of the film is the difference between the oxygen vacancy flux at the metal-oxide interface (which leads to growth of the film into the metal) and the dissolution rate:

$$\frac{dL}{dt} = V_m (J_{V_o}(0) - J_d) \quad (5)$$

where V_m is the molar volume of the oxide. When $J_{V_o}(0) = J_d$, the steady-state film thickness is achieved, and we focus on this state rather than the transient that leads to the steady-state. At steady state, $L(t) = L_{ss}$, the steady-state film thickness, and both the metal-oxide and oxide-solution interfaces are moving toward the metal with velocity V . This means that we can transform the coordinates to the moving reference as $x' = x - Vt$, where x' is the moving reference frame coordinate. In this reference frame, the boundaries of the film are fixed at $x' = 0$ and $x' = L_{ss}$ and the time dependence of the boundary positions is eliminated. From now on, the analysis is carried out in this reference frame and the primes are dropped on the coordinate system for notational convenience.

4.2. Non-dimensionalization

We non-dimensionalize the equations to facilitate the solution of the governing equations and remove several of the explicit parameter dependencies. For simplicity, we assume that the diffusion coefficient for cations and anions is the same. In general the diffusion coefficient of cations and anions will differ, and we allow them to differ in the general model formulation (see Eq. (2)). Having only one diffusion coefficient value implies that there is only one time scale in the system, which simplifies our interpretation of the perturbation growth rates in Section 6. We choose a characteristic length equal to the Helmholtz layer thickness, δ_H which is generally small. The characteristic time scale thus follows from the diffusion coefficient and characteristic length scale. The non-dimensional variables are as follows:

$$\{x^*, y^*\} = \frac{\{x, y\}}{\delta_H}, \quad t^* = \frac{D}{\delta_H^2} t, \quad C_i^* = V_m C_i, \quad \phi^* = \frac{2\mathcal{F}}{RT} \phi \quad (6)$$

Any energy quantity that appears (such as when setting the concentration boundary conditions) is non-dimensionalized by RT . The rest of the paper will refer only to the non-dimensionalized variables, and the asterisks will be dropped for notational convenience. Wherever we refer to a dimensional quantity with dimensions of length, we use $\delta_H = 0.4$ nm.

4.3. Solution of the model equations

The non-dimensionalized solution for the potential in the oxide and Helmholtz layer are, respectively,

$$\phi_O = -\frac{V_A - \Delta\phi^{M/O}}{\epsilon^r + L} x + V_A - \Delta\phi^{M/O} \quad (7a)$$

$$\phi_H = \phi_O(L)(L + 1 - x) \quad (7b)$$

For the purposes of describing the steady-state, the most important quantities are the electric field in the oxide, $\mathbf{E} = -\nabla\phi_O$

and the potential drop at the oxide-solution interface, which is simply $\phi_O(L)$. The electric field in the oxide is

$$\mathbf{E} = \frac{V_A - \Delta\phi^{M/O}}{\epsilon^r + L} \mathbf{i} \quad (8)$$

The transport equations $\nabla \cdot \mathbf{J}_j = 0$, when nondimensionalized and cast into the moving reference frame, have the following form:

$$\nabla^2 C_{V_o} + \nabla C_{V_o} \cdot \nabla \phi_O + V \frac{\partial C_{V_o}}{\partial x} = 0 \quad (9a)$$

$$\nabla^2 C_{V_m} - \nabla C_{V_m} \cdot \nabla \phi_O + V \frac{\partial C_{V_m}}{\partial x} = 0 \quad (9b)$$

For the planar film, the boundary conditions we use are those given in Table 1 with $\kappa_1 = \kappa_2 = 0$, since the interfacial energy has no effect for planar interfaces. The oxygen and cation vacancy profiles for the 1D planar state are

$$C_{V_o} = A \exp \left[- \left(\frac{\partial \phi_O}{\partial x} + V \right) x \right] + B \quad (10a)$$

$$A = \frac{C_{V_o}(L) - C_{V_o}(0)}{\exp \left[- \left(\frac{\partial \phi_O}{\partial x} + V \right) L \right] - 1} \quad (10b)$$

$$B = \frac{C_{V_o}(0) \exp \left[- \left(\frac{\partial \phi_O}{\partial x} + V \right) L \right] - C_{V_o}(L)}{\exp \left[- \left(\frac{\partial \phi_O}{\partial x} + V \right) L \right] - 1} \quad (10c)$$

and

$$C_{V_m} = A' \exp \left(\left(\frac{\partial \phi_O}{\partial x} - V \right) x \right) + B' \quad (11a)$$

$$A' = \frac{C_{V_m}(L) - C_{V_m}(0)}{\exp \left(\left(\frac{\partial \phi_O}{\partial x} - V \right) L \right) - 1} \quad (11b)$$

$$B' = \frac{C_{V_m}(0) \exp \left(\left(\frac{\partial \phi_O}{\partial x} - V \right) L \right) - C_{V_m}(L)}{\exp \left(\left(\frac{\partial \phi_O}{\partial x} - V \right) L \right) - 1} \quad (11c)$$

where $\partial\phi_O/\partial x$ can be found from Eq. (7a). Using Eqs. (2), (10) and (11) in Eq. (5), we can obtain an equation for $dL/dt = 0$. This is a non-linear equation for the steady-state film thickness, $L = L_{ss}$, which we determine numerically. The resulting non-linear equation is:

$$\left[-\frac{\partial C_{V_o}}{\partial x} - C_{V_o} \frac{\partial \phi_O}{\partial x} \right]_{x=0} = J_d |_{x=L_{ss}} \quad (12)$$

where C_{V_o} is given by Eq. (10), the velocity is $V = -J_d$, and the concentrations in J_d are evaluated using the boundary conditions in Table 1 for the oxide-solution interface located at $x = L_{ss}$.

4.4. Parameters

In order to utilize the model and compute L_{ss} as a function of applied potential, V_A , and solution pH, we must specify several parameters, including the dielectric constant ratio, ϵ^r , standard-state interfacial reaction free energy changes, $\Delta\mu_i^\circ$, metal-oxide interface potential drop, $\Delta\phi^{M/O}$, and dissolution rate constant, k_{diss} . Of particular importance are the reaction free energy changes

(equivalent to equilibrium constants), since they play a vital role in setting the defect concentrations, and choosing values arbitrarily can lead to unphysically small or large vacancy concentrations and non-charge-neutral lattices. We take the values of the free energy changes such that the defect concentrations in the film are nominally 10^{-3} mol. frac. at pH 4, which is reasonably consistent with defect concentrations deduced from Mott-Schottky analyses of passive films [44], and well with in the range of defect concentrations listed in Ref. [45]. We note that in order for the bulk film to be charge neutral, the following conditions must be met: $C_{V_M}(0) = C_{V_O}(L)$ and $C_{V_O}(0) = C_{V_M}(L)$. If this condition is not met, then for an oxide MO, the bulk cation and oxygen vacancy concentrations are unequal and the assumption of charge neutrality is broken. In order to ensure this condition is met, we calculate $\Delta\mu_2^+$ and $\Delta\mu_4^+$ based on the values on $C_{V_M}(0)$ and $C_{V_O}(0)$. The parameters that we ultimately choose are listed in Table 2. The dissolution rate constants k were chosen so that the computed film thicknesses were in the range 1–100 nm at pH = 4. These are given in terms of the diffusion coefficient D , since we work with the non-dimensional rate constants which are normalized by D . Unambiguously defining parameters is very difficult due to the lack of model experiments that aim to measure these fundamental constants.

4.5. Steady-state film thicknesses under various anodizing conditions

Using the parameters in Table 2, we compute the value of the steady-state film thickness, L_{SS} as a function of V_A and pH, for $\delta = 2$. These results are shown in Fig. 3 for both the PDM (Fig. 3a–c) and Vetter (Fig. 3d–f) dissolution rate laws. For both rate laws, the model predicts that L_{SS} increases linearly with increasing V_A . This behavior is consistent with experimental observations [47] and

the prediction from the PDM [10]. Furthermore, we predict that L_{SS} increases with increasing bulk solution pH, which is also consistent with experimental observations [47]. We find that L_{SS} increases exponentially with pH, which is due to the fact that pH is a logarithmic scale and we have assumed from the stoichiometry that the order of the dissolution reaction with respect to protons is 2. Thus, as pH is increased, the dissolution rate decreases exponentially and the film can grow to much larger thicknesses before $J_{V_O}(0) = J_{diss}(L_{SS})$. While not shown in Fig. 3, a linear increase in L_{SS} with V_A is found for $\delta = 1$ or 3, only the computed film thicknesses change. For $\delta = 1$, larger film thicknesses are found, while for $\delta = 3$ smaller film thicknesses are found. We found that for pH = 3 (not shown), the computed film thickness were unphysically small, which points to the fact that the passive state may not exist due to fast oxide dissolution kinetics.

5. Linear stability analysis

Since the model parameters lead to reasonable film thicknesses (above pH 3), and the behavior of L_{SS} with respect to V_A and pH is qualitatively consistent with experimental observations, we can investigate how a perturbation in the shape of interfaces evolves for both of the dissolution mechanisms considered. To reiterate, we do not consider the source of the perturbation when conducting the analysis. The perturbation could correspond some microstructural inhomogeneity; the only requirement is that the size of the perturbation is small. We consider the linear stability of the interfaces, and thus this approach only gives information about the very initial stages of an instability. The full interfacial evolution after the instability requires a numerical treatment using level-set or phase-field methods.

5.1. Introduction of the perturbation

We perturb the 1D system as shown in Fig. 4. The perturbations are described as follows:

$$h_1(y, t) = 0 + \hat{h}_1 \exp(iky + \sigma t) \quad (13a)$$

$$h_2(y, t) = L_{SS} + \hat{h}_2 \exp(iky + \sigma t) \quad (13b)$$

$$\phi_O = \bar{\phi}_O + \hat{\phi}_O(x) \exp(iky + \sigma t) \quad (13c)$$

$$\phi_H = \bar{\phi}_H + \hat{\phi}_H(x) \exp(iky + \sigma t) \quad (13d)$$

$$C_{V_O} = \bar{C}_{V_O} + \hat{C}_{V_O}(x) \exp(iky + \sigma t) \quad (13e)$$

$$C_{V_M} = \bar{C}_{V_M} + \hat{C}_{V_M}(x) \exp(iky + \sigma t) \quad (13f)$$

Here, the quantities with hats are the perturbation eigenfunctions, and those with bars correspond to the solution of the planar 1D model with oxide thickness L_{SS} . \hat{h}_1 and \hat{h}_2 are the amplitudes of the shape perturbations at the metal-oxide and oxide-solution interfaces respectively, and both are $\ll 1$. They are particularly important since all of the perturbation eigenfunctions can be written as functions of \hat{h}_1 and \hat{h}_2 . The goal of the morphological stability analysis is to solve for the perturbation eigenfunctions and determine the value of σ . If $\sigma > 0$ the perturbations grow in time and the passive film is morphologically unstable. If $\sigma < 0$ for all k , then the planar geometry is stable, while if σ is complex, then traveling waves are possible. Once σ is known, the ratio \hat{h}_1/\hat{h}_2 can be

Table 2
Parameter values input to our oxide growth model.

Parameter	Value
(a) PDM Dissolution Mechanism	
e^f	1.5
T/K	300
$\Delta\mu_1^+/Jmol^{-1}$	1.55×10^4
$\Delta\mu_2^+/Jmol^{-1}$	3.62×10^4
$\Delta\mu_3^+/Jmol^{-1}$	-1.5×10^4
$\Delta\mu_4^+/Jmol^{-1}$	5.52×10^4
$a_{M^{n+}}$	10^{-6} [46]
$k_d^P/m^{10}mol^{-3} s^{-1}$	$8.87 \times 10^9 D$
$\Delta\phi^{M/O}/V$	0.001 [11]
χ	2
V_A/V	0–0.5
pH	4–6
δ	1, 2, or 3
(b) Vetter Dissolution Mechanism	
e^f	1.5
T/K	300
$\Delta\mu_1^+/Jmol^{-1}$	1.55×10^4
$\Delta\mu_2^+/Jmol^{-1}$	3.24×10^4
$\Delta\mu_3^+/Jmol^{-1}$	-1.5×10^4
$\Delta\mu_4^+/Jmol^{-1}$	4.98×10^4
$a_{M^{n+}}$	10^{-6} [46]
$k_d^V/m^7mol^{-3} s^{-1}$	$1.88 \times 10^{14} D$
$\Delta\phi^{M/O}/V$	0.001 [11]
χ	2
V_A/V	0–0.5
pH	4–6
δ	2

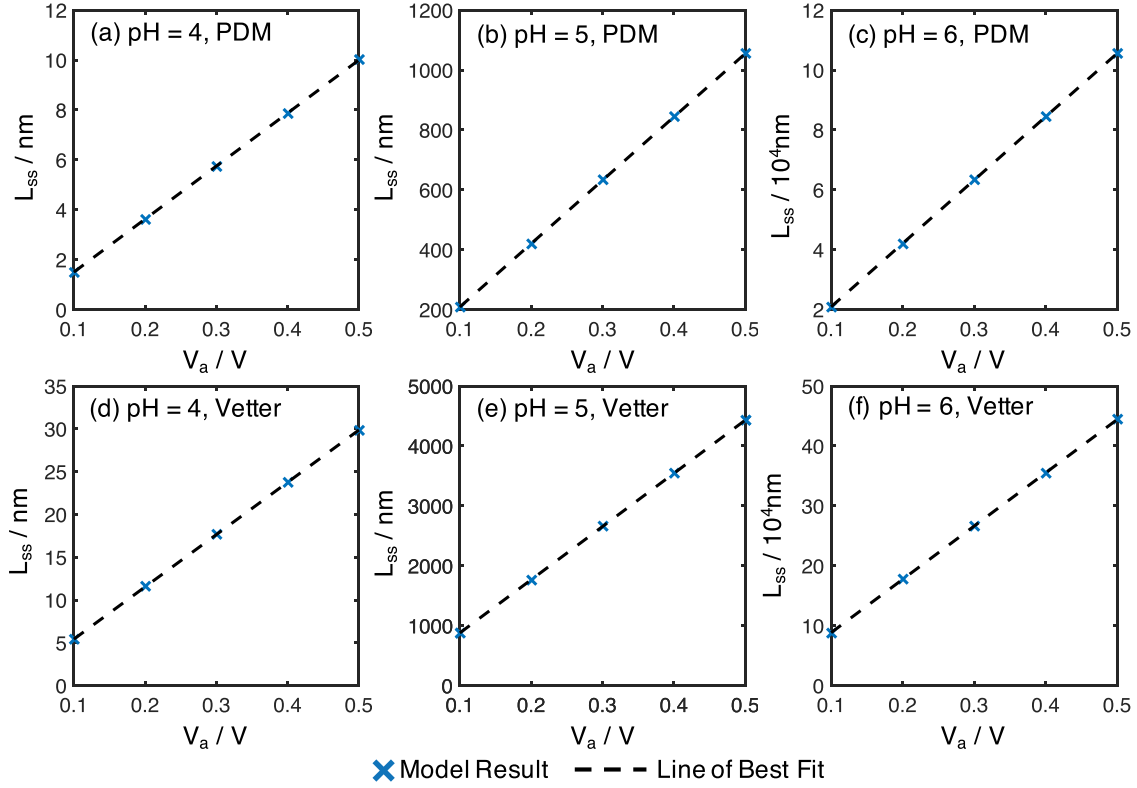


Fig. 3. Variations of the steady state film thickness L_{ss} vs. V_a and pH. Calculated film thicknesses are shown as blue x's, while the dashed line is a linear fit to the data. The results are shown for $\delta = 2$ and results for pH = 4, 5, and 6 are shown. (a)–(c) correspond to the PDM dissolution rate law and $\delta = 2$, while (d)–(f) correspond to the Vetter dissolution mechanism and $\delta = 2$. (For interpretation of the references to colour in this figure legend, the reader is referred to the Web version of this article.)

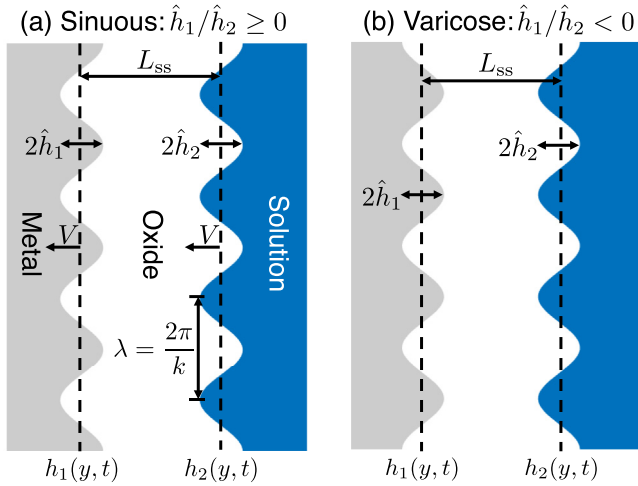


Fig. 4. Schematic showing the perturbed passive oxide film with all important quantities labeled. (a) depicts a sinuous perturbation meaning $\hat{h}_1/\hat{h}_2 \geq 0$. (b) depicts a varicose perturbation, meaning $\hat{h}_1/\hat{h}_2 < 0$. λ and V are the same for both the sinuous and varicose perturbation.

determined. The sign of \hat{h}_1/\hat{h}_2 indicates whether the interface perturbations are sinuous or varicose (see Fig. 4). The sinuous perturbation is characterized $\hat{h}_1/\hat{h}_2 \geq 0$ and the varicose mode is characterized by $\hat{h}_1/\hat{h}_2 < 0$.

Inserting Eq. (13) into the governing equations for the potential ($\nabla^2 \phi = 0$) and vacancy concentrations (Eq. (9)) yields the following equations for the perturbation eigenfunctions:

$$\frac{\partial^2 \hat{\phi}_O}{\partial x^2} - k^2 \hat{\phi}_O = 0 \quad (14a)$$

$$\frac{\partial^2 \hat{\phi}_H}{\partial x^2} - k^2 \hat{\phi}_H = 0 \quad (14b)$$

$$\frac{\partial^2 \hat{C}_{V_o}}{\partial x^2} + \left(\frac{\partial \bar{\phi}_O}{\partial x} + V \right) \frac{\partial \hat{C}_{V_o}}{\partial x} - k^2 \hat{C}_{V_o} = - \frac{\partial \bar{C}_{V_o}}{\partial x} \frac{\partial \hat{\phi}_O}{\partial x} \quad (14c)$$

$$\frac{\partial^2 \hat{C}_{V_M}}{\partial x^2} + \left(V - \frac{\partial \bar{\phi}_O}{\partial x} \right) \frac{\partial \hat{C}_{V_M}}{\partial x} - k^2 \hat{C}_{V_M} = - \frac{\partial \bar{C}_{V_M}}{\partial x} \frac{\partial \hat{\phi}_O}{\partial x} \quad (14d)$$

Here, we keep only the terms that are first order with respect to the perturbation amplitudes, and thus neglect terms that involve products of the perturbed potential and perturbed concentration fields, for example.

5.2. Linearized boundary conditions

In order to solve for the perturbation eigenfunctions, the boundary conditions must be linearized to reflect the presence of the interface perturbations. In order to do this, we must define the interface normal vectors and curvatures. Thermodynamics dictates that we choose an outward pointing normal to define the curvature of the oxide phase and thus the normal vector for the metal-oxide and oxide-solution interfaces point in opposite directions. At the metal-oxide interface, the normal vector is $\mathbf{n}_1 = ik\hat{h}_1 \exp(iky + \sigma t)\mathbf{i} - \mathbf{j}$ and the curvature is $\kappa_1 = \nabla \cdot \mathbf{n}_1 = -$

$\hat{h}_1 k^2 \exp(iky + \sigma t)$. At the oxide-solution interface, the normal vector is $\mathbf{n}_2 = -ik\hat{h}_2 \exp(iky + \sigma t)\mathbf{i} + \mathbf{j}$, and the curvature is $\kappa_2 = \nabla \cdot \mathbf{n}_2 = \hat{h}_2 k^2 \exp(iky + \sigma t)$.

The linearized boundary conditions for the potential are:

$$\hat{\phi}_O = -\hat{h}_1 \frac{\partial \bar{\phi}_O}{\partial x}, \text{ at } x = 0 \quad (15a)$$

$$\frac{\partial \hat{\phi}_H}{\partial x} - \epsilon^r \frac{\partial \hat{\phi}_O}{\partial x} = 0 \text{ at } x = L_{ss} \quad (15b)$$

$$\hat{\phi}_H = \hat{\phi}_O + \hat{h}_2 \left(\frac{\partial \bar{\phi}_O}{\partial x} - \frac{\partial \bar{\phi}_H}{\partial x} \right) \text{ at } x = L_{ss} \quad (15c)$$

$$\hat{\phi}_H = -\hat{h}_2 \frac{\partial \bar{\phi}_H}{\partial x} \text{ at } x = L_{ss} + 1 \quad (15d)$$

The linearized boundary conditions for the concentration perturbations are:

$$\begin{aligned} \hat{C}_{V_o} = \hat{h}_1 \left(\left(\exp[-\Delta\mu_1^* + \Delta\phi^{M/O}] \right) \right. \\ \left. + 2\exp[\Delta\mu_3^* - \Delta\mu_1^*] \right) \gamma^{M/O} k^2 - \frac{\partial \bar{C}_{V_o}}{\partial x} \Big) \text{ at } x = 0 \end{aligned} \quad (16a)$$

$$\begin{aligned} \hat{C}_{V_o} = -\bar{C}_{V_o} \left(\hat{\phi}_O + \hat{h}_2 \frac{\partial \bar{\phi}_O}{\partial x} + \gamma^{O/S} \hat{h}_2 k^2 \right) \\ - \hat{h}_2 \frac{\partial \bar{C}_{V_o}}{\partial x} \text{ at } x = L_{ss} \end{aligned} \quad (16b)$$

$$\hat{C}_{V_M} = \hat{h}_1 \left(\bar{C}_{V_M} \gamma^{M/O} k^2 - \frac{\partial \bar{C}_{V_M}}{\partial x} \right) \text{ at } x = 0 \quad (16c)$$

$$\begin{aligned} \hat{C}_{V_M} = \bar{C}_{V_M} \left[\frac{\delta}{2} \left(\hat{\phi}_O + \hat{h}_2 \frac{\partial \bar{\phi}_O}{\partial x} \right) - \gamma^{O/S} \hat{h}_2 k^2 \right] \\ - \hat{h}_2 \frac{\partial \bar{C}_{V_M}}{\partial x} \text{ at } x = L_{ss} \end{aligned} \quad (16d)$$

Note that for the stability analysis, we now include the interfacial energy terms since, for $k > 0$, the interfaces have curvature and the Gibbs-Thomson effect is relevant. The surface energy has no effect if the film remains planar ($k = 0$), unlike in the analyses of passivity breakdown by Sato [6] and Heuer [8]. The non-dimensionalized interfacial energy is defined as $\gamma^* = \bar{V}\gamma/(\delta_{\text{Helm}}RT)$, and we have chosen $\gamma^{M/O} = \gamma^{O/S} = 0.4 \text{ J/m}^2$. The value of 0.4 J/m^2 was chosen based on the work of Marks [4] and roughly equal to the calculated oxide-solution interface energy for the $\text{Al}_2\text{O}_3(001)$ surface. The metal-oxide interface energy that we employ is likely low based on the values calculated by DFT [48,49], which indicate that this energy greater than 1 J/m^2 for Al_2O_3 interfaces with Al, Ag, Cu and Ni. This means that we are likely underestimating the metal-oxide interface energy and thus are underestimating the stability of that interface.

The derivation of the linearized boundary conditions for the concentration perturbations are given in Appendix B, and the solutions to the perturbation eigenfunctions are given in Appendix C.

5.3. Perturbation growth rate, σ

The growth rate of the perturbation is found by considering how

the velocities of the metal-oxide and oxide-solution interfaces are perturbed by the presence of the shape perturbations. The velocities of the interfaces are found from the following equations:

$$V_1 = \frac{dh_1}{dt} = -J_{V_o}(h_1) \quad (17a)$$

$$V_2 = \frac{dh_2}{dt} = -J_d(h_2) \quad (17b)$$

Taking the derivatives and utilizing the perturbation eigenfunctions in the dissolution rate laws J_d , it is possible to show that the perturbed interface velocity can be written as the following system of equations

$$\sigma \hat{h}_1 + \hat{J}_{V_o}(h_1) = 0 \quad (18a)$$

$$\sigma \hat{h}_2 + \hat{J}_{\text{diss}}(h_2) = 0 \quad (18b)$$

where $\hat{J}_{V_o}(h_1)$ is the perturbed oxygen vacancy flux and the metal-oxide interface and $\hat{J}_d(h_2)$ is the perturbed dissolution rate.

The perturbed vacancy flux at the M/O interface $\hat{J}_{V_o}(h_1)$ is given by the expression

$$\begin{aligned} \hat{J}_{V_o}(h_1) = \left[- \left(\frac{\partial \hat{C}_{V_o}}{\partial x} + \hat{h}_1 \frac{\partial^2 \bar{C}_{V_o}}{\partial x^2} \right) - \bar{C}_{V_o} \frac{\partial \hat{\phi}_O}{\partial x} \right. \\ \left. - \left(\hat{C}_{V_o} + \hat{h}_1 \frac{\partial \bar{C}_{V_o}}{\partial x} \right) \frac{\partial \bar{\phi}_O}{\partial x} \right]_{x=0} \end{aligned} \quad (19)$$

The perturbed dissolution flux from the PDM rate law is

$$\begin{aligned} \hat{J}_d^P = \left[J_d^P \alpha \left(\frac{\delta}{2} - 1 \right) \left(\hat{\phi}_O + \hat{h}_2 \frac{\partial \bar{\phi}_O}{\partial x} \right) - k_d^P \left((1 - \bar{C}_{V_M}) \left(\hat{C}_{V_o} + \hat{h}_2 \frac{\partial \bar{C}_{V_o}}{\partial x} \right) \right. \right. \\ \left. \left. + (1 - \bar{C}_{V_o}) \left(\hat{C}_{V_M} + \hat{h}_2 \frac{\partial \bar{C}_{V_M}}{\partial x} \right) \right) \times C_{H^+}^2 \exp \left(\alpha \left(\frac{\delta}{2} - 1 \right) \bar{\phi}_O \right) \right]_{x=L_{ss}} \end{aligned} \quad (20)$$

while the perturbed dissolution flux from the Vetter rate law is:

$$\begin{aligned} \hat{J}_d^V = \left[\hat{J}_d^V \alpha \frac{\delta}{2} \left(\hat{\phi}_O + \hat{h}_2 \frac{\partial \bar{\phi}_O}{\partial x} \right) \right. \\ \left. - k_d^V \left(\hat{C}_{V_M} + \hat{h}_2 \frac{\partial \bar{C}_{V_M}}{\partial x} \right) C_{H^+}^2 \exp \left(\alpha \frac{\delta}{2} \bar{\phi}_O \right) \right]_{x=L_{ss}} \end{aligned} \quad (21)$$

Regardless of the choice of the dissolution rate law, it is possible to the cast the perturbed velocity system (Eq. (18)) into the matrix form

$$\begin{pmatrix} \sigma + f_1(k) & f_2(k) \\ f_3(k) & \sigma + f_4(k) \end{pmatrix} \begin{pmatrix} \hat{h}_1 \\ \hat{h}_2 \end{pmatrix} = 0 \quad (22)$$

Here the functions f_1 , f_2 , f_3 , and f_4 are complicated (but analytical) functions associated with either the perturbed vacancy flux (f_1 and f_2) or perturbed dissolution flux (f_3 and f_4). In order to find a non-trivial solution, the determinant of the coefficient matrix must equal zero, which yields a quadratic equation for $\sigma(k)$. With $\sigma(k)$ known, we can solve for the ratio \hat{h}_1/\hat{h}_2 . Since there are two solutions for $\sigma(k)$, we expect that one of the solutions corresponds to the sinuous perturbation ($\hat{h}_1/\hat{h}_2 \geq 0$) and the other corresponds to the varicose perturbation ($\hat{h}_1/\hat{h}_2 < 0$). For the parameters we

choose, we find that the discriminant of the quadratic equation for $\sigma(k)$ is always greater than 0 and thus we do not find any imaginary roots that would correspond to a traveling wave instability. Analytical expressions for $\sigma(k)$ have been obtained using *Mathematica*, but are rather long and cumbersome write down and as such they will not be given here.

5.4. Stability dispersion curves $\sigma(k)$

For investigations of the stability of the system, we use the parameters listed in Table 2 and fix the pH at 4. This is because at this pH value, the calculated steady state film thicknesses are of the same order of magnitude as those measured in experiments. At lower pH values, the film thicknesses are sub-nanometers, while for higher pH values the film thicknesses are on the scale of microns, much thicker than naturally formed passive films. We break the analysis of stability into 3 cases: (i) $\delta = 1$, (ii) $\delta = 2$ and (iii) $\delta = 3$. For each of the cases, we examine the stability behavior as a function of V_A , for both the PDM and Vetter dissolution mechanisms. For the Vetter dissolution mechanism, the stability curves have the same general shape regardless of the value of δ , so for this mechanism we only show plots for $\delta = 2$, since for an oxide MO, it is most likely that the cation has the same charge in the oxide and solution (e.g. NiO [42]).

When considering the two roots of the quadratic equation for $\sigma(k)$, we find that one of the solutions (corresponding to subtracting

the discriminant) gives $\hat{h}_1/\hat{h}_2 < 0$ for all k , V_A , and δ . This solution corresponds to a purely varicose perturbation and has $\sigma(k) < 0$ for all k , indicating that this solution is unconditionally stable. Since we are primarily interested in the instabilities that may be present, we will not discuss this solution further. In what follows, the dispersion curves are given in terms of the non-dimensional variables and as such do not have units. Quantities involving the length scale are dimensionalized assuming $\delta_H = 0.4$ nm.

5.4.1. PDM dissolution mechanism

The stability dispersion curves for the sinuous mode as a function of V_A and δ are shown in Fig. 5. First, we note that $\sigma = 0$ and $\hat{h}_1/\hat{h}_2 = 1$ at $k = 0$ for all values of V_A and δ , which indicates that translating the planar passive film in space does not affect its stability. We also note that the dispersion curves themselves are essentially independent of V_A . For $\delta = 1$ and $\delta = 2$, we find that $\sigma < 0$ for all k , which means that perturbations of the passive film shape are unconditionally stable. For $\delta = 3$, corresponding to oxidative dissolution of the film, we find an instability is present, where $\sigma > 0$. The max growth rate of the perturbation corresponds to a wavelength of ≈ 1.3 nm, assuming a Helmholtz layer thickness of $\delta_H = 0.4$ nm.

The ratio \hat{h}_1/\hat{h}_2 is also plotted as an inset in Fig. 5. The curves show $\hat{h}_1/\hat{h}_2 \rightarrow 0$ as $k \rightarrow \infty$. Fig. 6 illustrates how the plots of \hat{h}_1/\hat{h}_2 give the expected morphology of the film interfaces. In all cases, $\sigma >$

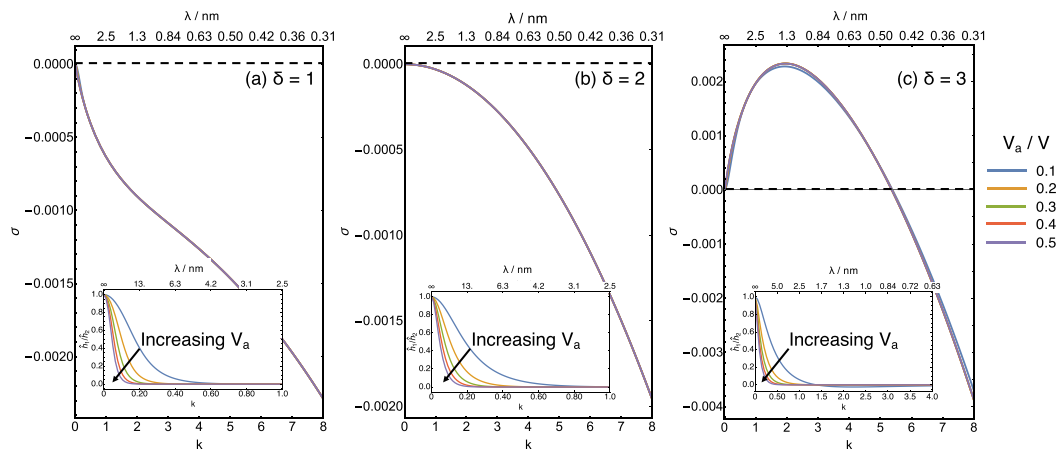


Fig. 5. Stability dispersion curves as a function of δ and V_{app} for the PDM dissolution mechanism. The inset plot shows, the ratio \hat{h}_1/\hat{h}_2 . An instability is found for $\delta > 2$, corresponding to oxidative dissolution of the passive film in the PDM framework.

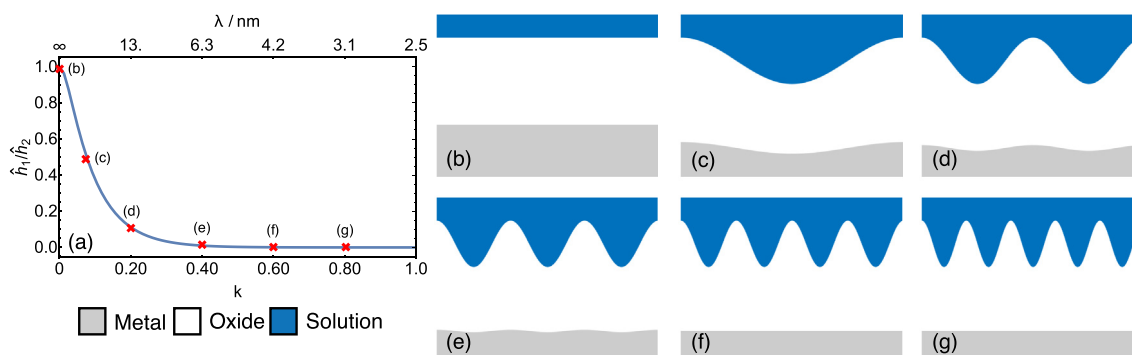


Fig. 6. Illustration of how the plot of \hat{h}_1/\hat{h}_2 gives an indication of the expected film morphology. (a) shows \hat{h}_1/\hat{h}_2 vs. k for $\delta = 3$ and $V_A = 0.5$ V. The red x's and their labels correspond to the images in (b)–(g). As k increases from 0, the perturbation wavelength decreases and the metal-oxide interface becomes increasingly flat. The figures in (b)–(g) are rotated 90° counterclockwise with respect to the coordinate system depicted in Fig. 4. (For interpretation of the references to colour in this figure legend, the reader is referred to the Web version of this article.)

0 except for Fig. 6b, which is the $k = 0$ case. Fig. 5 shows that the wavenumber with the maximum growth rate is about $k = 2$. Since this perturbation has the max growth rate, this is the perturbation wavenumber that is most likely to be observed in the linear regime. The figure indicates that for this wavenumber, the morphology of the film will be similar to what is shown in Fig. 6g. As k increases from 0, the wavelength of the perturbation decreases, while the amplitude of the metal-oxide interface perturbation also decreases. For large enough k , the metal-oxide interface is essentially flat, and the shape perturbation exists only at the oxide-solution interface.

From Fig. 5c, we note that for $\delta = 3$ and the smallest V_A shown (0.1 V), \hat{h}_1/\hat{h}_2 does become negative around $k = 1.5$. This means that it may be possible to support an unstable varicose perturbation. However, the corresponding steady-state film thickness in these conditions is 0.3 nm, which is quite thin and may not correspond to a uniform passivating film but perhaps discrete oxide nuclei on the surface. The origin of the change in behavior for this very thin film is the fact that the perturbed fields at the interfaces interact in the bulk portion of the film. For the thicker films at higher V_A , the field perturbations decay away from the interfaces sufficiently fast that the two interfaces do not interact.

5.4.2. Vetter dissolution mechanism

Fig. 7 shows the dispersion curves that result from the Vetter dissolution rate law. As before, the curves are essentially the same regardless of the value of V_A . At $k = 0$, $\sigma = 0$ and $\hat{h}_1/\hat{h}_2 = 1$, which again confirms the translational invariance of the system under consideration. Fig. 7 shows the dispersion curves for $\delta = 2$ and indicates the max growth rate of the perturbation occurs at a perturbation wavelength of ≈ 1.3 nm. The instability is present and the dispersion curves have the same shape for any $\delta > 0$.

The ratio \hat{h}_1/\hat{h}_2 for the Vetter dissolution mechanism is also plotted as the inset in Fig. 7. As for the PDM mechanism, the plot

implies that when the instability is triggered, the metal-oxide interface will remain essentially planar, since \hat{h}_1/\hat{h}_2 is essentially 0 except for very small k (long wavelength) perturbations.

6. Discussion

6.1. Mechanism of the instability

Having established the presence of instability in the passive film growth model, we now turn to identifying the mechanism driving the instability. In Fig. 8 we plot the perturbed dissolution rate and the perturbed oxygen vacancy flux at the metal/oxide interface as a function of k for both the PDM and Vetter dissolution mechanisms. These plots can be interpreted as follows: when the perturbed quantity is negative, that quantity is increased in the troughs of the perturbed interface, while it is decreased at the peaks of the perturbed interface. For dissolution, the negative perturbed dissolution rate indicates that the troughs of the oxide-solution interface will dissolve faster than the peaks of that interface, and the non-planar oxide-solution interface will become more exaggerated over time. A similar argument can be made for the perturbed oxygen vacancy flux at the metal-oxide interface. We note that in Fig. 8b and $V_A = 0.1$ V, the perturbed oxygen vacancy flux at the metal-oxide interface does become positive, indicating that the vacancy flux will tend to stabilize that planar interface. This case, as discussed previously, corresponds to a very small L_{ss} such that this behavior may never be observed.

The plots in Fig. 8 indicate that the changes in the dissolution rate at the oxide-solution interface are orders of magnitude larger than the changes in the vacancy flux at the metal-oxide interface, which implies that the instability is dominated by dissolution of the oxide. This instability supports the localized thinning model for film breakdown [1,16]. The shape of the perturbed dissolution rate curves matching those of the unstable dispersion curves shown in Figs. 5 and 7 lends additional support to the idea that the instability is dominated by locally enhanced dissolution of the troughs.

The reason for the enhancement of the dissolution rate in the troughs of the perturbed oxide-solution interface can be found by plotting the perturbed potential through the Helmholtz layer, as shown in Fig. 9. The plot indicates that perturbation leads to an increase in the Helmholtz layer potential drop in the troughs, which serves to increase the dissolution rate there. This effect dominates over the changes in the vacancy concentrations at small k , but at large k the concentration changes dominate and capillary effects stabilize the planar film. The perturbed potential drop is independent of the dissolution mechanism considered. The primary conclusion that we make is that any oxide whose dissolution rate increases with increasing Helmholtz layer potential drop will experience the instability described here.

6.2. Morphology evolution

Fig. 10 shows how the interfacial morphology is expected to evolve shortly after the onset of the instability, depicting the increasingly nonplanar interfaces. In this figure, the arrows denotes the total velocities of the interfaces, not the perturbed velocities. Thus, the net direction of interface motion is still toward the metal in the presence of the perturbations, and the mean interface position moves downward in time, as depicted. The magnitudes of the arrows denote the relative magnitude of the interface velocities. Since the perturbed dissolution rate is much greater than the perturbed oxygen vacancy flux at the metal-oxide interface, we can see that the morphology change occurs predominantly at the oxide-solution interface. In Fig. 10, the amplitude of the metal-oxide

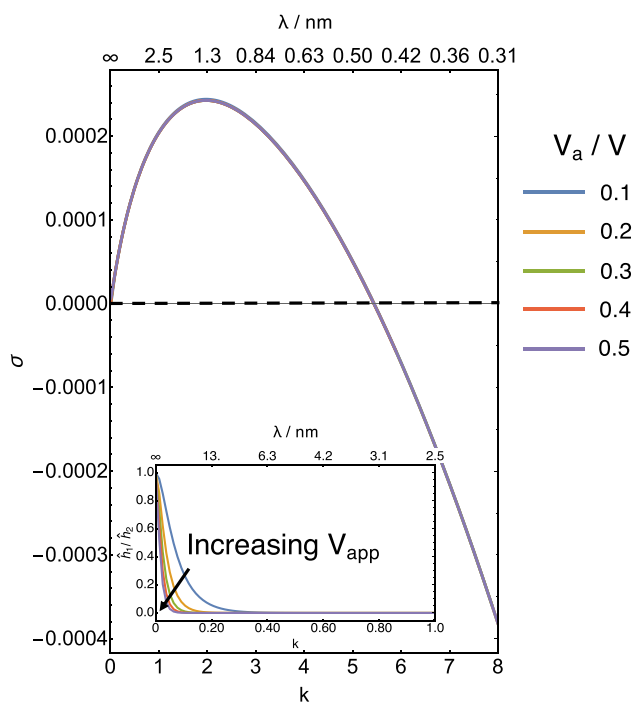


Fig. 7. Stability dispersion curves for the Vetter dissolution mechanism as a function of V_A for $\delta = 2$. The instability is found for any $\delta > 0$. The inset plot shows \hat{h}_1/\hat{h}_2 .

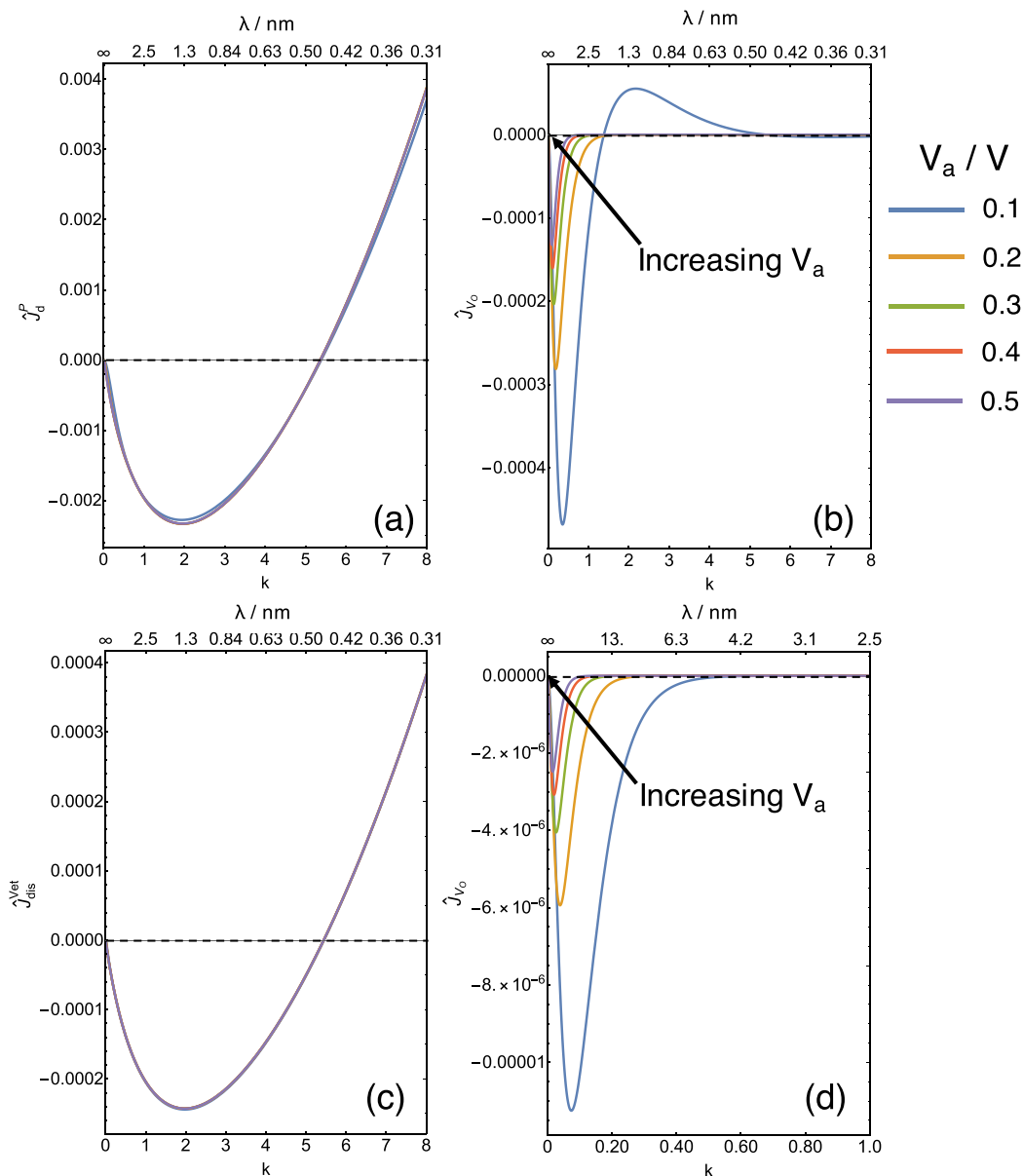


Fig. 8. Plots of the (a) perturbed dissolution rate \hat{J}_d^p , and (b) perturbed oxide growth rate \hat{J}_{vo} for the PDM dissolution mechanism, as well as the (c) perturbed dissolution \hat{J}_d^{vet} and (d) perturbed oxide growth rate for the Vetter dissolutions mechanism. These plots are only given for the case where an instability is present, that is for $\delta = 3$ for (a) and (b) and $\delta = 2$ for (c) and (d).

interface perturbation is exaggerated so that the morphology development at that interface can be visualized.

Since we have only considered linear stability, we do not know whether the unstable dissolution at the oxide-solution interface will expose the underlying metal to the solution. There remains a distinct possibility that the complete interfacial evolution leads to a new steady-state passive film with nonplanar interfaces. Future work with phase-field simulations will aim to address the long-term evolution of morphology after the onset of the instability.

6.3. Perturbation time scale

In the previous section, we were able to identify the length of the instability at ≈ 1.3 nm since δ_H is known to be small, and a value of 0.4 nm was used as discussed previously. Defining the time scale of the perturbation is far more difficult. This is because time was

non-dimensionalized by the diffusion coefficient D , which is difficult to determine for passive oxide films. While diffusion data for bulk oxides does exist, the defect concentrations in passive films can be orders magnitude larger than in bulk oxides [45], and thus diffusion coefficients in passive films would be expected to be larger than in the bulk films.

The growth rate of the instability is given at the maximum in the $\sigma(k)$ curves. Figs. 5 and 7 indicate that the max growth rate of the perturbations is between 2×10^{-4} and 2×10^{-3} . This means that the time constant, τ , for the instability, is between $8 \times 10^{-17} \text{ m}^2/D$ and $8 \times 10^{-16} \text{ m}^2/D$. Diffusion coefficients in passive films have been calculated for WO_3 from experimental data using the PDM [44], as well as for Cr_2O_3 using density functional theory (DFT) calculations [50]. The PDM analysis indicates that the diffusion coefficient in WO_3 films is in the range $3.7 - 5.3 \times 10^{-19} \text{ m}^2/\text{s}$, while the DFT calculations indicate that the diffusion coefficient in

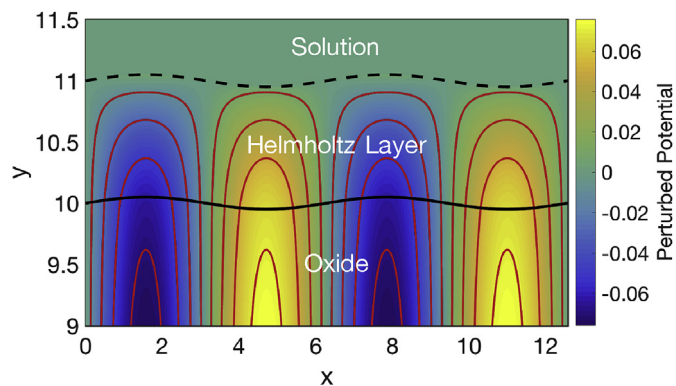


Fig. 9. Plot of the perturbed potential at the oxide-solution interface. The red line are equipotentials, meant to give an indication of the direction of the perturbed electric field. At the troughs of the interface, the potential drop through the Helmholtz layer is increased. (For interpretation of the references to colour in this figure legend, the reader is referred to the Web version of this article.)

Cr_2O_3 is in the range $8.6 \times 10^{-23} - 10^{-18} \text{ m}^2/\text{s}$. Using these values of the diffusivity, this suggests that τ is between 800 s and 9.3×10^6 s. We note that these values are very material dependent, and it is possible that for certain materials the diffusion coefficients may be larger and reduce the time constants for the instability.

Since the diffusivities in passive films have not been analyzed for a wide variety of oxide materials, a survey of the literature on diffusion coefficients in the bulk oxides MgO, NiO, and Al_2O_3 indicates that the bulk vacancy diffusion coefficient at 300 K can range anywhere from 10^{-64} to $10^{-16} \text{ m}^2/\text{s}$ Refs. [51–59]. This bounds the value of τ between 8×10^{-5} s and 8×10^{48} s. This large variance in the time constant indicates that the small value will yield a rapidly growing instability, and the latter value corresponds to an instability that will not be observable.

6.4. Connection to pit initiation models

Finally, we would like to make an explicit connection to the literature on pitting corrosion, especially the dependencies on presence of the chloride and oxidizers in the environment. Frankel [1] has noted that the presence of oxidizers in the solution exacerbates the problem of pitting corrosion, and our analysis predicts that oxidizing dissolution (i.e. chromia dissolution in the presence of permanganate, a strong oxidizing agent [60]) is inherently unstable.

It is also known that the chloride concentration plays a roll in determining the pitting behavior of a passive film. This could be due to adsorption of chloride ions catalytically enhancing dissolution,

or chloride incorporation into the passive film leading to voiding at the metal/oxide interface [3]. Okada has shown that chloride adsorption to the oxide-solution interface and subsequent complexation with the cations in the oxide film leads to a dissolution rate that increases with increasing oxide-solution potential drop [24]. When this happens, we would expect the breakdown instability that we describe here. We also note that DFT calculations have shown that chloride adsorption on some oxides leads to a reduction of the oxide-solution interface energy [4]. Reduction of the surface energy leads to larger perturbation growth rate and a wider range of unstable wavenumbers in cases where an instability exists, as shown in Fig. 11. The reduction of the surface energy is greater at larger Cl^- concentrations.

With respect to the localized nature of the passive film breakdown, the work of Marks [4] shows that in general the surface energy variation due to chloride adsorption is a strong function of the orientation of the oxide surface, with some orientations

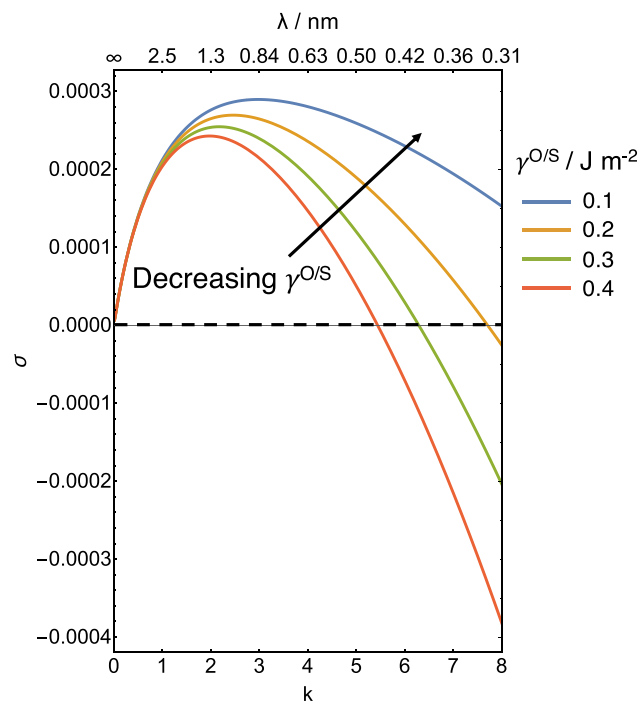


Fig. 11. Comparison of the stability dispersion curves for the Vetter rate law as the surface energy γ is varied. The parameters used are listed in Table 2, with pH = 4 and $\delta = 2$. The growth rate of the perturbations increases as γ decreases.

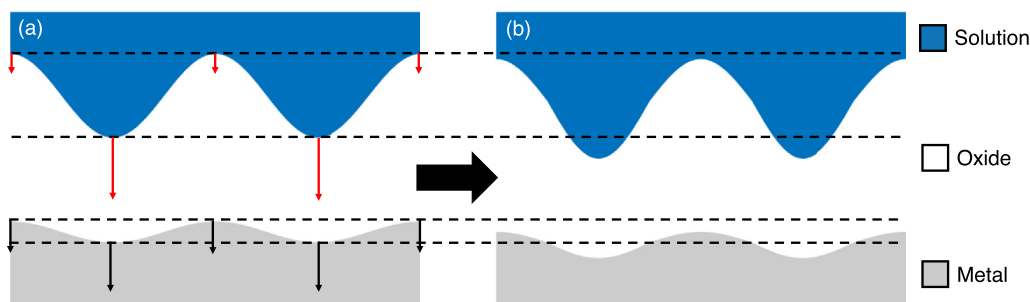


Fig. 10. Expected evolution of the interfacial morphological shortly after the onset of the instability. (a) shows the initial state of the system, with a morphological perturbation present. The arrows show the relative magnitudes and directions of the interfacial velocities. (b) shows the interfacial morphology a short time after the instability in (a) is triggered. The black-dashed lines are meant to guide the eye. The non-planarity of the interfaces becomes increasingly exaggerated because of the instability.

showing greater reductions in the surface energy than others (e.g. the (100) surface of Al_2O_3 shows much greater reduction in surface energy than the (001) surface. This heterogeneity in the surface energy reduction suggests that certain grains of the oxide film will be more vulnerable to breakdown due to Cl^- adsorption and the resulting morphological instability. Furthermore, our analysis does not include a trigger for the shape perturbation, which could correspond to some localized damage or flaw in the oxide film as other models have proposed. If the initial perturbation is localized, then the subsequent film thinning due to the instability will be localized as well. Furthermore, any thinning of the film due to the instability, in the absence of a nonlinear steady-state, may eventually lead to the oxide locally dissolving away and will manifest as the initial breakdown step for pit initiation.

7. Summary

We have developed and analyzed the morphological stability of a model for the growth of a passive oxide film on a metal surface under potentiostatic conditions. The model for the growing planar film leads to a linear increase in the steady-state film thickness with applied potential V_A and an increase in the steady-state film thickness with increasing pH. Both of these results are consistent with experimental observations. The linear morphological stability analysis finds that, depending on the parameters and dissolution mechanism, the passive oxide film may be unstable to shape perturbations which grow exponentially in time. Dissolution of the passive film is unstable for the PDM oxide dissolution mechanism if the cation is oxidized upon being ejected to solution. If cation ejection is the rate limiting step for oxide dissolution, then the passive film is always morphologically unstable. We find that the results are consistent with the literature on oxide film breakdown in the presence of chloride ions, and that passivity breakdown may be a morphological instability in the passive film. Our results also imply that one-dimensional models for passive film formation can be inapplicable in broad classes of corrosion processes. Our analysis is unique in that it predicts *both* the size and time scales of the breakdown event. The analysis provides insight into the mechanisms responsible for the formation of non-planar films and potentially the formation of a pit or pore in the oxide.

Acknowledgements

The authors would like to acknowledge support from the Office of Naval Research MURI Understanding Atomic Scale Structure in Four Dimensions to Design and Control Corrosion Resistant Alloys under Grant No. N00014-16-1-2280. The authors would also like to thank Prof. John R. Scully and Prof. Laurence D. Marks for helpful discussions regarding passive film dissolution and the role of chloride ions.

List of Symbols

$\phi, \bar{\phi}, \hat{\phi}$	Potential, unperturbed potential, perturbed potential
V_A	Potential applied to the metal relative to the bulk solution potential
$\Delta\phi^{M/O}$	Potential drop at the metal-oxide interface
ϵ^r	Ratio of the dielectric constants of the oxide and Helmholtz layer ($\epsilon_{\text{oxide}}/\epsilon_{\text{Helm}}$)
δ_H	Thickness of the Helmholtz layer
C, \bar{C}, \hat{C}	Vacancy concentration, unperturbed vacancy concentration, perturbed vacancy concentration
D	Vacancy diffusion coefficient
z_j	charge number of species j

\mathcal{F}	Faraday's constant
$\Delta\mu_i^\circ$	Standard state change in chemical potential for reaction i as numbered in Fig. 1
χ, δ	Charge of the cation in the oxide and solution respectively
$a_{M^{i+}}$	Activity of cations in solution
J_d^P, J_d^V	Dissolution flux for the PDM and Vetter dissolution mechanisms, respectively
V_m	Molar volume of the oxide
V	Velocity of the interfaces in the steady-state
L, L_{SS}	thickness of the film, thickness of the unperturbed film
\hat{h}_1, \hat{h}_2	Perturbation amplitudes at the metal-oxide and oxide-solution interfaces, respectively
σ	Growth rate of the perturbation
k	Wavenumber of the perturbation
κ_1, κ_2	curvature of the metal-oxide and oxide-solution interfaces, respectively

Appendix A. Derivation of boundary conditions with structure conservation and the Gibbs-Thomson effect

Including the structure conservation requirement and Gibbs-Thomson Effect in the boundary conditions is very straightforward. Here we will derive the boundary condition for the cation vacancy concentration at the metal-oxide interface. The approach is the same for the remaining concentration boundary conditions.

The reaction we are considering is $m + V_M^\times \rightleftharpoons M_M + \chi e^-$. Following from Macdonald [10], we first consider the chemical potentials of all species involved in the reaction, assuming an ideal solution model for the chemical potentials.

$$\tilde{\mu}_m = \mu_m^\circ \quad (\text{A.1a})$$

$$\tilde{\mu}_{V_M} = \mu_{V_M}^\circ + RT \ln(C_{V_M}) + \bar{V}\gamma^{M/O}\kappa_1 - \chi\mathcal{F}\phi_0(h_1) \quad (\text{A.1b})$$

$$\tilde{\mu}_{M_M} = \mu_{M_M}^\circ + RT \ln(1 - C_{V_M}) \quad (\text{A.1c})$$

$$\tilde{\mu}_e = \mu_e^\circ - \mathcal{F}\phi_m \quad (\text{A.1d})$$

Here $\tilde{\mu}_j$ represents the electrochemical potential of species j , μ_j° is the standard state chemical potential of species j , \bar{V} is the partial molar volume of the vacancy, $\gamma^{M/O}$ is the energy of the metal-oxide interface, and κ_1 is the curvature of the metal-oxide interface. Here we note two things. First, the chemical potentials of V_M and M_M are coupled together by the structure conservation requirement. Setting $C_{M_M} = 1 - C_{V_M}$ ensures that the cation vacancy concentration cannot exceed the site density of the cation sublattice. The second thing to note is the presence of the term $\bar{V}\gamma^{M/O}\kappa_1$ for the electrochemical potential of cation vacancies. This term accounts for how capillarity at a non-planar interface modifies the vacancy chemical potential in accordance with the Gibbs-Thomson effect. For a planar metal-oxide interface, $\kappa_1 = 0$ and the interface energy has no effect.

To obtain the boundary condition in Table 1, we assume that the reaction is in the equilibrium. This means that $\sum_{\text{prod}} n_j \tilde{\mu}_j - \sum_{\text{react}} n_j \tilde{\mu}_j = 0$, where the n_j are the stoichiometric coefficients. Using the expressions in Eq. (A.1) in the equilibrium condition and rearranging terms, we arrive at the boundary condition

$$\frac{C_{V_M}}{1 - C_{V_M}} = \exp\left(\frac{\Delta\mu_3^\circ - \chi \mathcal{F} \Delta\phi^{M/O} - \bar{V} \gamma^{M/O} \kappa_1}{RT}\right) \quad (\text{A.2})$$

Appendix B. Linearized concentration boundary conditions

Here we will show the procedure for obtaining the linearized boundary condition for the cation vacancy concentration at the metal-oxide interface. In the non-dimensional variables, it is easy to show that

$$C_{V_M}(h_1) = \frac{1}{\exp(-\Delta\mu_3^\circ + \Delta\phi^{M/O} + \gamma\kappa) + 1} \quad (\text{B.1})$$

Since the expected defect concentration is expected to be small (order 10^{-2} or smaller), we can safely ignore the 1 in the denominator of the expression without affecting the results to obtain the approximate expression

$$C_{V_M}(h_1) = \exp(\Delta\mu_3^\circ - \Delta\phi^{M/O} - \gamma^{M/O} \kappa_1) \quad (\text{B.2})$$

Since $\kappa_1 = -\hat{h}_1 k^2 \exp(ikx + \sigma t)$ and $\hat{h}_1 \ll 1$, we can expand the exponential as

$$C = -\hat{h}_1 \frac{(V_A - \Delta\phi^{M/O}) e^r \cosh[k(L_{SS} + 1)]}{(L_{SS} + \epsilon^r)(e^r \cosh(kL_{SS}) \sinh(k) + \cosh(k) \sinh(kL_{SS}))} + \hat{h}_2 \frac{(V_A - \Delta\phi^{M/O}) e^r (1 + \epsilon^r - (\epsilon - 1)(\cosh(k) - \cosh(2kL_{SS}) + \cosh(k + 2kL_{SS})))}{(L_{SS} + \epsilon^r)(e^r \cosh(kL_{SS}) \sinh(k) + \cosh(k) \sinh(kL_{SS}))} \quad (\text{C.1c})$$

$$\begin{aligned} C_{V_M}(h_1) &= \exp(\Delta\mu_3^\circ - \Delta\phi^{M/O}) (1 - \gamma^{M/O} \kappa_1) \\ &= \bar{C}_{V_M}(0) - \bar{C}_{V_M}(0) \gamma^{M/O} \kappa_1 \\ &= \bar{C}_{V_M}(0) + \bar{C}_{V_M}(0) \gamma^{M/O} \hat{h}_1 k^2 \exp(ikx + \sigma t) \end{aligned} \quad (\text{B.3})$$

Now, we can Taylor expand the left hand side of this equations as follows

$$\begin{aligned} C_{V_M}(h_1) &= C_{V_M}(0) + (h_1 - 0) \frac{\partial C_{V_M}}{\partial x} \Big|_{x=0} \\ &= \bar{C}_{V_M}(0) + \hat{C}_{V_M}(0) \exp(ikx + \sigma t) + \hat{h}_1 \exp(ikx + \sigma t) \frac{\partial \bar{C}_{V_M}}{\partial x} \Big|_{x=0} \end{aligned} \quad (\text{B.4})$$

Here we have only kept terms that are linear with respect to \hat{h}_1 . Combining Eqs. B.3 and B.4 and rearranging we obtain the linearized boundary condition

$$\hat{C}_{V_M}(0) = \hat{h}_1 \left(\bar{C}_{V_M}(0) \gamma^{M/O} k^2 - \frac{\partial \bar{C}_{V_M}}{\partial x} \Big|_{x=0} \right) \quad (\text{B.5})$$

A similar procedure is followed for the remaining boundary conditions, except at the oxide-solution interface, we must also Taylor expand $\phi_{\text{oxide}}(h_2)$ about $x = L_{SS}$.

Appendix C. Perturbation eigenfunctions

The perturbation eigenfunctions are needed to evaluate the perturbed oxygen vacancy and dissolution fluxes in order to compute $\sigma(k)$. These solutions are given here:

Appendix C.1. Potential perturbation eigenfunctions

The general solution to the perturbed oxide potential is $\phi_O(x) = A \sinh(kx) + B \cosh(kx)$ and the general solution to the perturbed Helmholtz layer potential is $\phi_H = C \cosh(kx) + D \sinh(kx)$. Plugging these expressions into the linearized boundary conditions we find that the coefficients are

$$A = -\hat{h}_1 \frac{(V_A - \Delta\phi^{M/O}) (\cosh(k) \cosh(kL_{SS}) + \epsilon^r \sinh(k) \sinh(kL_{SS}))}{(L_{SS} + \epsilon^r) (\epsilon^r \cosh(kL_{SS}) \sinh(k) + \cosh(k) \sinh(kL_{SS}))} - \hat{h}_2 \frac{(V_A - \Delta\phi^{M/O}) ((\epsilon^r - 1) \cosh(k) - \epsilon^r)}{(L_{SS} + \epsilon^r) (\epsilon^r \cosh(kL_{SS}) \sinh(k) + \cosh(k) \sinh(kL_{SS}))} \quad (\text{C.1a})$$

$$B = \hat{h}_1 \frac{(V_A - \Delta\phi^{M/O})}{L_{SS} + \epsilon^r} \quad (\text{C.1b})$$

$$D = \hat{h}_1 \frac{(V_A - \Delta\phi^{M/O}) e^r \sinh[k(L_{SS} + 1)]}{(L_{SS} + \epsilon^r) (\epsilon^r \cosh(kL_{SS}) \sinh(k) + \cosh(k) \sinh(kL_{SS}))} + \hat{h}_2 \frac{(V_A - \Delta\phi^{M/O}) (\epsilon^r - 1) e^r (\sinh[k(L_{SS} + 1)] - \sinh(kL_{SS}))}{(L_{SS} + \epsilon^r) (\epsilon^r \sinh(k) + \cosh(k) \tanh(kL_{SS}))} \quad (\text{C.1d})$$

Appendix C.2. Concentration perturbation eigenfunctions

The solution for the concentration perturbation eigenfunctions is significantly complicated by the inhomogeneous nature of the governing equations. The homogeneous solutions have the form

$$\hat{C}_{V_O} = Fe^{r_+ x} + Ge^{r_- x} + \hat{C}_{V_O}^P \quad (\text{C.2a})$$

$$\hat{C}_{V_M} = He^{s_+ x} + Ie^{s_- x} + \hat{C}_{V_M}^P \quad (\text{C.2b})$$

where

$$r_{\pm} = \frac{-(V + \partial_y \bar{\phi}_O) \pm \sqrt{(V + \partial_y \bar{\phi}_O)^2 + 4k^2}}{2} \quad (\text{C.3a})$$

$$s_{\pm} = \frac{-(V - \partial_y \bar{\phi}_O) \pm \sqrt{(V - \partial_y \bar{\phi}_O)^2 + 4k^2}}{2} \quad (\text{C.3b})$$

and $\hat{C}_{V_0}^P$ and $\hat{C}_{V_M}^P$ are the particular solutions satisfying the inhomogeneous governing equations. The particular solutions to the inhomogeneous problems and the unknown coefficients F , G , H and I were found using *Mathematica*. The closed form analytical solutions are rather long and complex and not given here.

References

- [1] G.S. Frankel, Pitting corrosion of metals: a review of the critical factors, *J. Electrochem. Soc.* 145 (6) (1998) 2186, <https://doi.org/10.1149/1.1838615>.
- [2] T.P. Hoar, W.R. Jacob, Breakdown of passivity of stainless steel by Halide ions, *Nature* 216 (12) (1967) 1299–1301, <https://doi.org/10.1038/2161299a0>.
- [3] L.F. Lin, C.Y. Chao, D.D. Macdonald, A point defect model for anodic passive films: II. Chemical breakdown and pit initiation, *J. Electrochem. Soc.* 128 (6) (1981) 1194, <https://doi.org/10.1149/1.2127592>.
- [4] L. Marks, Competitive chloride chemisorption disrupts hydrogen bonding networks: DFT, crystallography, thermodynamics and morphological consequences, *Corrosion* 74 (3) (2017) 295–311.
- [5] Z. Szklarska-Smialowska, Mechanism of pit nucleation by electrical breakdown of the passive film, *Corros. Sci.* 44 (5) (2002) 1143–1149, [https://doi.org/10.1016/S0010-938X\(01\)00113-5](https://doi.org/10.1016/S0010-938X(01)00113-5).
- [6] N. Sato, A theory for breakdown of anodic oxide films on metals, *Electrochim. Acta* 16 (10) (1971) 1683–1692, [https://doi.org/10.1016/0013-4686\(71\)85079-X](https://doi.org/10.1016/0013-4686(71)85079-X).
- [7] Y. Tang, R. Ballarini, A theoretical analysis of the breakdown of electrostrictive oxide film on metal, *J. Mech. Phys. Solid.* 59 (2) (2011) 178–193, <https://doi.org/10.1016/j.jmps.2010.11.002>.
- [8] A.H. Heuer, H. Kahn, P.M. Natishan, F.J. Martin, L.E. Cross, Electrostrictive stresses and breakdown of thin passive films on stainless steel, *Electrochim. Acta* 58 (1) (2011) 157–160, <https://doi.org/10.1016/j.electacta.2011.09.027>.
- [9] C.Y. Chao, L.F. Lin, D.D. Macdonald, A point defect model for anodic passive films: I. Film growth kinetics, *J. Electrochem. Soc.* 128 (6) (1981) 1187, <https://doi.org/10.1149/1.2127591>.
- [10] D.D. Macdonald, M. Urquidí-Macdonald, Theory of steady-state passive films, *J. Electrochem. Soc.* 137 (8) (1990) 2395–2402, <https://doi.org/10.1149/1.2086949>.
- [11] A. Seyeux, V. Maurice, P. Marcus, Oxide film growth kinetics on metals and alloys: I. Physical model, *J. Electrochem. Soc.* 160 (6) (2013) C189–C196, <https://doi.org/10.1149/2.036306jes>.
- [12] V. Battaglia, J. Newman, Modeling of a growing oxide film: the iron/iron oxide system, *J. Electrochem. Soc.* 142 (5) (1995) 1423, <https://doi.org/10.1149/1.2048591>.
- [13] C. Bataillon, F. Bouchon, C. Chainais-Hillairet, C. Desgranges, E. Hoarau, F. Martin, S. Perrin, M. Tupin, J. Talandier, Corrosion modelling of iron based alloy in nuclear waste repository, *Electrochim. Acta* 55 (15) (2010) 4451–4467, <https://doi.org/10.1016/j.electacta.2010.02.087>.
- [14] S. Dewitt, K. Thornton, Model for anodic film growth on aluminum with coupled bulk transport and interfacial reactions, *Langmuir* 30 (18) (2014) 5314–5325, <https://doi.org/10.1021/la500782d>.
- [15] A. Couet, A.T. Motta, A. Ambar, The coupled current charge compensation model for zirconium alloy fuel cladding oxidation: I. Parabolic oxidation of zirconium alloys, *Corros. Sci.* 100 (2015) 73–84, <https://doi.org/10.1016/j.corsci.2015.07.003>.
- [16] P. Marcus, V. Maurice, H.H. Strehblow, Localized corrosion (pitting): a model of passivity breakdown including the role of the oxide layer nanostructure, *Corros. Sci.* 50 (9) (2008) 2698–2704, <https://doi.org/10.1016/j.corsci.2008.06.047>.
- [17] N. Sato, Anodic breakdown of passive films on metals, *J. Electrochem. Soc.* 129 (2) (1982) 255, <https://doi.org/10.1149/1.2123808>.
- [18] J.S. Langer, Instabilities and pattern formation in crystal growth, *Rev. Mod. Phys.* 52 (1) (1980) 1–28, <https://doi.org/10.1103/RevModPhys.52.1>. arXiv: 1011.1669v3.
- [19] R.F. Sekerka, S.R. Coriell, G.B. McFadden, *Morphological Stability*, second ed., vol. 1, Elsevier B.V., 2014 <https://doi.org/10.1016/B978-0-444-56369-9.00014-9>.
- [20] D. Du, D. Srolovitz, Electrostatic field-induced surface instability, *Appl. Phys. Lett.* 85 (21) (2004) 4917–4919, <https://doi.org/10.1063/1.1826233>.
- [21] D. Srolovitz, On the stability of surfaces of stressed solids, *Acta Metall.* 37 (2) (1989) 621–625, [https://doi.org/10.1016/0001-6160\(89\)90246-0](https://doi.org/10.1016/0001-6160(89)90246-0).
- [22] B.J. Spencer, P.W. Voorhees, S.H. Davis, Morphological instability in epitaxially strained dislocation-free solid films: linear stability theory, *J. Appl. Phys.* 73 (10) (1993) 4955–4970, <https://doi.org/10.1063/1.353815>.
- [23] K.A. Wu, P.W. Voorhees, Morphological instability of ferromagnetic thin films, *J. Appl. Phys.* 106 (7), <https://doi.org/10.1063/1.3239989>.
- [24] T. Okada, A theory of perturbation-initiated pitting, *J. Electrochem. Soc.* 132 (3) (1985) 537, <https://doi.org/10.1149/1.2113883>.
- [25] C. Wagner, Oxidation of alloys involving noble metals, *J. Electrochem. Soc.* 103 (10) (1956) 571, <https://doi.org/10.1149/1.2430159>.
- [26] R.W. Balluffi, S.M. Allen, W.C. Carter, *Kinetics of Materials*, John Wiley & Sons, Inc., Hoboken, NJ, 2005.
- [27] G.K. Singh, A.A. Golovin, I.S. Aranson, V.M. Vinokur, Formation of nanoscale pore arrays during anodization of aluminum, *Eur. Lett.* 70 (6) (2005) 836–842, <https://doi.org/10.1209/epl/i2005-10039-9>.
- [28] G.K. Singh, A.A. Golovin, I.S. Aranson, Formation of self-organized nanoscale porous structures in anodic aluminum oxide, *Phys. Rev. B Condens. Matter Mater. Phys.* 73 (20) (2006) 1–12, <https://doi.org/10.1103/PhysRevB.73.205422>.
- [29] L.G. Stanton, A.A. Golovin, Effect of electrostriction on the self-organization of porous nanostructures in anodized aluminum oxide, *Math. Model Nat. Phenom.* 3 (5) (2008) 73–91, <https://doi.org/10.1051/mmnp:2008077>.
- [30] L.G. Stanton, A.A. Golovin, Effect of ion migration on the self-assembly of porous nanostructures in anodic oxides, *Phys. Rev. B Condens. Matter Mater. Phys.* 79 (3) (2009) 1–7, <https://doi.org/10.1103/PhysRevB.79.035414>.
- [31] J. Tersoff, Y. Tu, G. Grinstein, Effect of curvature and stress on reaction rates at solid interfaces, *Appl. Phys. Lett.* 73 (16) (1998) 2328–2330, <https://doi.org/10.1063/1.121812>.
- [32] C.H.P. Lupis, *Chemical Thermodynamics of Materials*, Elsevier Science Publishing Co., Inc., 1983.
- [33] P. Marcus (Ed.), *Corrosion Mechanisms in Theory and Practice*, third ed., CRC Press, 2017.
- [34] A. Atkinson, Transport processes during the growth of oxide films at elevated temperature, *Rev. Mod. Phys.* 57 (2) (1985) 437–470, <https://doi.org/10.1103/RevModPhys.57.437>.
- [35] C. Wagner, Beitrag zur Theorie des Anlaufvorgangs, *Z. Phys. Chem.* 21B (1) (1933) 25–41, <https://doi.org/10.1515/zpch-1933-2105>.
- [36] N. Cabrera, N.F. Mott, Theory of the oxidation of metals, *Rep. Prog. Phys.* 12 (1) (1949) 163–184, <https://doi.org/10.1088/0034-4885/12/1/308>.
- [37] M. Vankeerberghen, 1D steady-state finite-element modelling of a bi-carrier one-layer oxide film, *Corros. Sci.* 48 (11) (2006) 3609–3628, <https://doi.org/10.1016/j.corsci.2006.01.013>.
- [38] K. Leistner, C. Toulemonde, B. Diawara, A. Seyeux, P. Marcus, Oxide film growth kinetics on metals and alloys: II. Numerical simulation of transient behavior, *J. Electrochem. Soc.* 160 (6) (2013) C197–C205, <https://doi.org/10.1149/2.037306jes>.
- [39] A.T. Fromhold, E.L. Cook, Kinetics of oxide film growth on metal crystals: electronic and ionic diffusion in large surface-charge and space-charge fields, *Phys. Rev.* 175 (3) (1968) 877–897, <https://doi.org/10.1103/PhysRev.175.877>.
- [40] M.H. Lankhorst, H.J. Bouwmeester, H. Verweij, Thermodynamics and transport of ionic and electronic defects in crystalline oxides, *J. Am. Ceram. Soc.* 80 (9) (1997) 2175–2198, <https://doi.org/10.1111/j.1151-2916.1997.tb03107.x>.
- [41] K.J. Vetter, F. Gorn, Kinetics of layer formation and corrosion processes of passive iron in acid solutions, *Electrochim. Acta* 18 (4) (1973) 321–326, [https://doi.org/10.1016/0013-4686\(73\)80036-2](https://doi.org/10.1016/0013-4686(73)80036-2).
- [42] C. Ludvig, W.H. Casey, On the mechanisms of dissolution of bunsenite[NiO(s)] and other simple oxide minerals, *J. Colloid Interface Sci.* 178 (1996) 176–185.
- [43] N. Sato, G. Okamoto, Anodic passivation of nickel in sulfuric acid solutions, *J. Electrochem. Soc.* 110 (6) (1963) 605, <https://doi.org/10.1149/1.2425838>.
- [44] E. Sikora, J. Sikora, D.D. Macdonald, A new method for estimating the diffusivities of vacancies in passive films, *Electrochim. Acta* 41 (6) (1996) 783–789, [https://doi.org/10.1016/0013-4686\(95\)00312-6](https://doi.org/10.1016/0013-4686(95)00312-6).
- [45] J.W. Schultze, M.M. Lohrengel, Stability, reactivity and breakdown of passive films. Problems of recent and future research, *Electrochim. Acta* 45 (15–16) (2000) 2499–2513, [https://doi.org/10.1016/S0013-4686\(00\)00347-9](https://doi.org/10.1016/S0013-4686(00)00347-9).
- [46] E. Stansbury, R. Buchanan, *Fundamentals of Electrochemical Corrosion*, ASM International, Materials Park, Ohio, 2000.
- [47] N. Sato, T. Noda, Ion migration in anodic barrier oxide films on iron in acidic phosphate solutions, *Electrochim. Acta* 22 (8) (1977) 839–843, [https://doi.org/10.1016/0013-4686\(77\)80007-8](https://doi.org/10.1016/0013-4686(77)80007-8).
- [48] W. Zhang, J.R. Smith, Nonstoichiometric interfaces and Al₂O₃ adhesion with Al and Ag, *Phys. Rev. Lett.* 85 (15) (2000) 3225–3228, <https://doi.org/10.1103/PhysRevLett.85.3225>.
- [49] W. Zhang, J.R. Smith, A.G. Evans, The connection between ab initio calculations and interface adhesion measurements on metal/oxide systems: Ni/Al₂O₃ and Cu/Al₂O₃, *Acta Mater.* 50 (15) (2002) 3803–3816, [https://doi.org/10.1016/S1359-6454\(02\)00177-5](https://doi.org/10.1016/S1359-6454(02)00177-5).
- [50] F. Lebreau, M.M. Islam, B. Diawara, P. Marcus, Structural, magnetic, electronic, defect, and diffusion properties of Cr₂O₃: a DFT+U study, *J. Phys. Chem. C* 118 (31) (2014) 18133–18145, <https://doi.org/10.1021/jp5039943>.
- [51] M.L. Volpe, J. Reddy, Cation Self-diffusion and semiconductivity in NiO, *J. Chem. Phys.* 53 (3) (1970) 1117–1125, <https://doi.org/10.1063/1.1674107>.
- [52] R. Lindner, G.D. Parfitt, Diffusion of radioactive magnesium in magnesium oxide crystals, *J. Chem. Phys.* 26 (1) (1957) 182–185, <https://doi.org/10.1063/1.1743247>.
- [53] Y. Ikeda, K. Nii, G. Beranger, P. Lacombe, Cation transport phenomena in NiO, *Trans. Japan Inst. Met.* 15 (6) (1974) 441–446, <https://doi.org/10.2320/matertrans1960.15.441>.

- [54] H.I. Yoo, B.J. Wuensch, W.T. Petuskey, Oxygen self-diffusion in single-crystal MgO: secondary-ion mass spectrometric analysis with comparison of results from gas-solid and solid-solid exchange, *Solid State Ionics* 150 (3–4) (2002) 207–221, [https://doi.org/10.1016/S0167-2738\(02\)00537-4](https://doi.org/10.1016/S0167-2738(02)00537-4).
- [55] A.E. Paladino, W.D. Kingery, Aluminum ion diffusion in aluminum oxide, *J. Chem. Phys.* 37 (5) (1962) 957–962, <https://doi.org/10.1063/1.1733252>.
- [56] B.J. Wuensch, W.C. Steele, T. Vasilos, Cation self-diffusion in single-crystal MgO, *J. Chem. Phys.* 5258 (1973) 5258–5266, <https://doi.org/10.1063/1.1679138>.
- [57] Y. Oishi, W.D. Kingery, Self-diffusion of oxygen in single crystal and polycrystalline aluminum oxide, *J. Chem. Phys.* 33 (2) (1960) 480–486, <https://doi.org/10.1063/1.1731170>.
- [58] M. O'Keefe, W.J. Moore, Diffusion of oxygen in single crystals of nickel oxide, *J. Phys. Chem.* 65 (8) (1961) 1438–1439, <https://doi.org/10.1021/j100826a039>.
- [59] T.P. Jones, R.L. Coble, C.J. Mogab, Defect diffusion in single crystal aluminum oxide, *J. Am. Ceram. Soc.* 52 (6) (1969) 331–334, <https://doi.org/10.1111/j.1151-2916.1969.tb11937.x>.
- [60] M.G. Segal, R.M. Sellers, Kinetics of metal oxide dissolution, *J. Chem. Soc., Faraday Trans.* 78 (1987) 1149–1164.